NANOPETROPHYSICAL CHARACTERIZATION OF THE UPPER MANCOS SHALE IN THE SAN JUAN BASIN, NEW MEXICO, U.S.A.

by:

Ann Kiat Gan

Presented to the Faculty of the Graduate School of The

University of Texas at Arlington in Partial Fulfillment of the

Requirements

for the Degree of

MASTER OF SCIENCE IN EARTH AND ENVIROMENTAL SCIENCES

THE UNIVERSITY OF TEXAS AT ARLINGTON

August 2022

Table of Contents

List of Figures

List of Tables

Abstract

The San Juan Basin is no stranger to oil and gas production and the Mancos Shale is one of the formations of the basin that had been producing petroleum since the early 1920's as conventional, and recently as, unconventional resources. Due to the economic significance of shale oil and gas production, oil and gas companies have a strong motivation to understand the petrophysical property measurements of shale reservoirs, in this case, the Upper Mancos Shale, both in the laboratory and in the subsurface. By understanding shale petrophysics, such as total organic carbon, mineral composition, wettability, porosity, permeability, pore connectivity for pore space at the nanometer scale, and understanding the pore structure of, and fluid migration, within the shale, these can be utilized to improve and optimize drilling practices to achieve the ultimate goal of enhanced wellbore stability and ultimately, increase shale oil and gas production and recovery.

In order to understand the nano-petrophysics of the Upper Mancos Shale with low porosity and extremely low permeability, which is critical in assessing the reservoir quality, a series of experiments will be performed in the laboratory on core samples. These experiments are low-pressure nitrogen physisorption, helium pycnometry for densities measurements, water immersion porosimetry after vacuum pulling, contact angle, and liquid imbibition. In addition, this thesis will obtain supplementary data for total organic carbon content, X-ray diffraction, and pyrolysis from GeoMark Research.

XRD analyses show that carbonate content increases in the northeastern part of the San Juan Basin, while the more silica-rich facies are found in the southwest region of the Basin. N_2 physisorption indicates that all the samples are microporous, mesoporous and macroporous, with macropores as the most dominant pore distribution. The majority of the samples was evenly

distributed between Argillaceous Siliceous Mudstone and Mixed Mudstone with six samples each. The maturation by Calculated Vitrinite Reflectance (% Ro) from T_{max} and TOC increases from the southwest to northeast region of the Basin, and there are high TOC contents on the east and west flank of the Basin. The fluid imbibition experiment shows that the samples have intermediate to well connectivity with hydrophilic fluid and well connectivity pore network with hydrophobic fluid, whereas the contact angle results show that all the samples are moderately strongly water wet and strongly oil wet. The helium pycnometry and 2DT vacuum saturation results show that the porosity decreases with depth, and there is an inverse relationship between porosity and bulk density from the 2DT vacuum saturation and helium pycnometry test.

Introduction

As of 2020, the U.S. Energy Information Administration (EIA) stated the state of New Mexico produced crude oil at 1,036 thousand barrels per day, and the natural gas gross withdrawals was 5,603 million cubic feet per day. According to the U.S. Department of Energy, the San Juan Basin has been producing oil and natural gas since the 1920's and it has one of the largest concentrations of natural gas reserves in the United States, where the production of natural gas started in 1921 by conventional wells, then by coal bed methane (CBM) wells in 1948, and the gas production only bloomed in the 1990's. However, it was reported that the gas production in this basin has been on the decline since 2006. As for the petroleum production in the San Juan Basin, there are several sources, which are naturally fractured shales, conventional sandstones, and coal bed methane reservoirs (Hu et al., 2019). With a low matrix porosity and permeability, the Mancos Shale can also be designated as an unconventional reservoir (Engler et al., 2001) The average undiscovered conventional oil and gas for the Upper Mancos Shale is six million barrels of oil (MMBO) and 51 billion cubic feet of gas (BCFG), while the average undiscovered continuous/unconventional gas for the Upper Mancos Shale is 2,649 BCFG. Oil and gas companies have been exploring the Mancos Shale and the Niobrara/Gallup sandstone in the San Juan Basin for oil resources development.

Due to the economic significance of shale oil and gas production, oil and gas companies have a strong motivation to understand the measurements of petrophysical properties for oil and gas shale, both in the laboratory and in the subsurface (Sondergeld, Newsham, Comisky, Rice, & Rai, 2010). The knowledge of shale petrophysics can be utilized to improve and optimize drilling practices to achieve enhanced wellbore stability (Al-Arfaj & Al-Kharaa, 2017) and the ultimate goal of increased shale oil and gas production and recovery. Therefore, the goals of this study is

to investigate the petrophysical properties of the Upper Mancos Shale such as total organic carbon (TOC), mineral composition, wettability, porosity, permeability, pore connectivity and more in the nanometer scale, understand the fluid migration within the shale pore networks, and to evaluate the quality of this reservoir. For this study, a total of 13 core samples from the following four different wells were obtained from the New Mexico Bureau of Geology & Mineral Resources (NMBGR): (Figure 1.) 11x30 (Mckinley County), Burnham 1 (San Juan County), Joan White 2 (San Juan County), and 148M (Rio Arriba County).

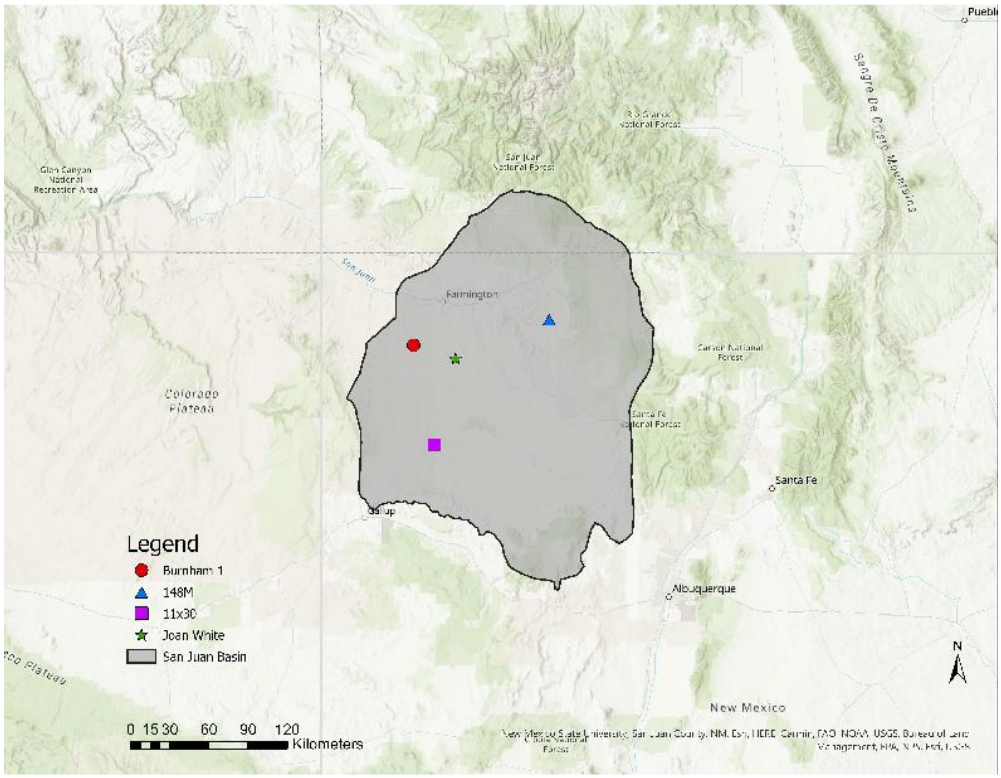

Figure 1. Well locations for 11x30 (Mckinley County), Burnham 1 (San Juan County), Joan White 2 (San Juan County), and 148M (Rio Arriba County).

Geologic Setting

The San Juan Basin (Figure 2) is located within the boundary of four states- New Mexico, Colorado, Arizona, and Utah (Wright, 1979) and has an area of approximately 21,600 square miles (Craigg, 2001). The basin structure, a circular, asymmetric structural depression, is 140 miles wide and 200 miles long (Craigg, 2001), located mainly in the east-central part of the Colorado Plateau. The San Juan Basin has been determined as a craton-accreted margin basin and a foredeep basin by Klemme (1986) and Bally (1975), respectively, where both of these types of basins consist of the same characteristics in that they are usually filled by sequences encompassing two or more cycles of deposition-first, a carbonate shelf/platform sediments cycle and a orogenic clastics cycle (Huffman Jr., 1987). The San Juan Basin have seen such sequences during the Paleozoic and Upper Cretaceous to Oligocene periods (Huffman Jr., 1987).

The northern margin of the San Juan Basin is bounded by the San Juan Uplift, with the northwest trending Gallina-Archuleta Arc bounding the northeast basin (Huffman Jr., 1987). The eastern margin of the basin is bounded by the Nacimiento Uplift, which is a north trending mountain block representing the southwestern border of the Rocky Mountains (Huffman Jr., 1987). The southeast margin of the San Juan Basin is bounded by the Rio Grande Rift, the Ignacio Monocline, and the Lucero Uplift and the northwest trending Zuni Uplift bounds the south-central margin of the basin. The southwest of the San Juan Basin is bounded by the "southwestern part of the Zuni Uplift and the southern end of the north-trending Defiance Uplift" (Huffman Jr., 1987). The northern part of the Defiance Uplift bounds the San Juan Basin along the western margin and this uplift divides the San Juan Basin and the Black Mesa Basin (Huffman Jr., 1987). The northwest of the basin is bounded by the Carrizo Mountains, Sleeping Ute Mountain, and the La Plata Mountains (Huffman Jr., 1987).

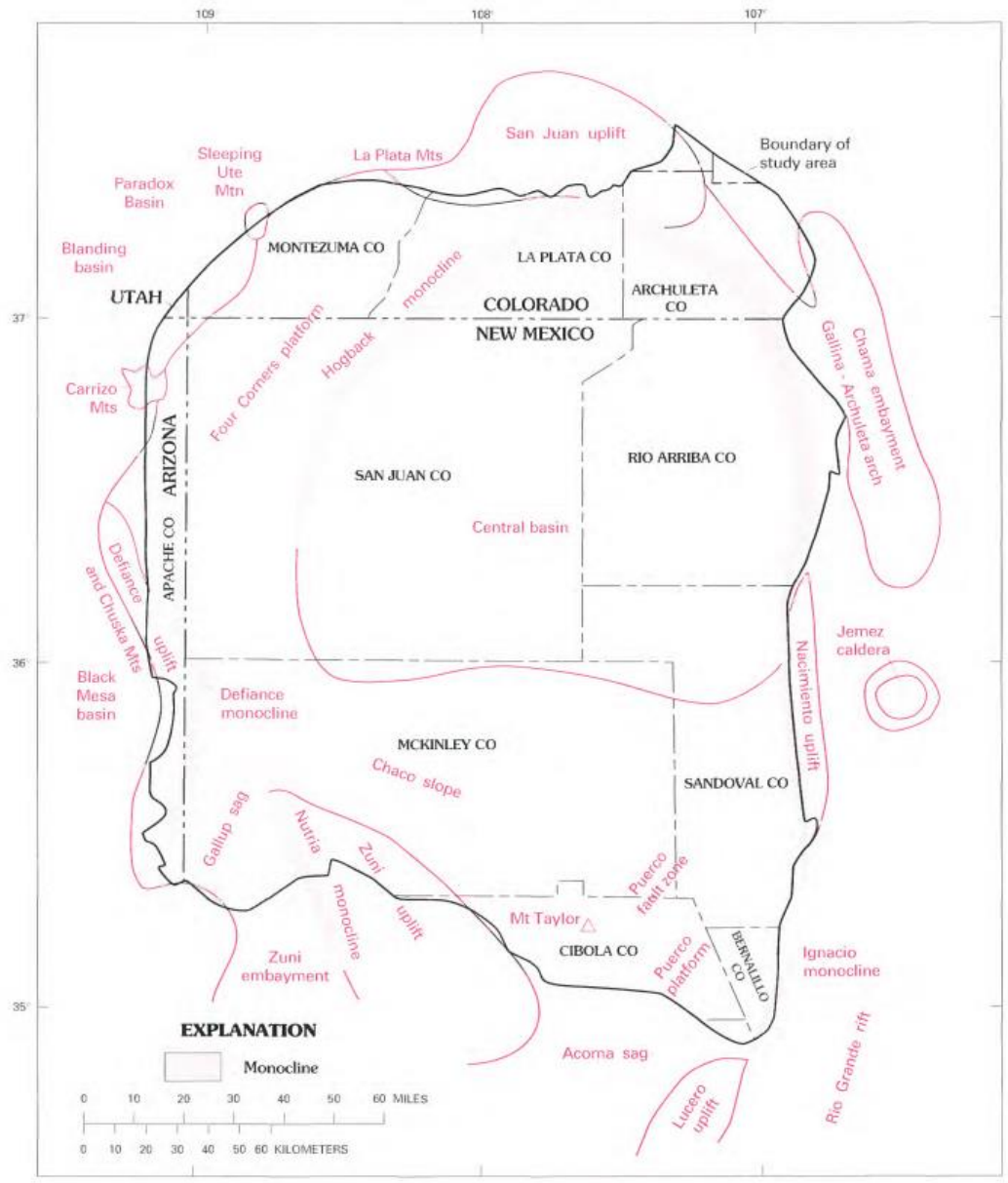

Figure 2. Geological setting of San Juan Basin

According to Kelley (1950, p. 101), the extensive tectonic evolution of the San Juan Basin started in the Precambrian with "complex metamorphism, deformation, intense erosion, and subsequent burial under Phanerozoic rocks". Tectonism happened in the late Paleozoic through Mesozoic period along the borders of the basin in the form of uplifts mentioned above (Huffman Jr., 1987). The structural elements presently seen in the San Juan Basin began forming

in the Latest Cretaceous and early Tertiary period (Huffman Jr., 1987). By the Late Cretaceous period, a large interior seaway, called . There was a scene of interplay between a shallow seaway on the northeast and a clastic sediment supply on the southwest in the San Juan Basin vicinity (Molenaar, 1977; Broadhead, 2015).

Figure 3. Western Interior Seaway

The northwest-to-southeast-trending shoreline of the sea in northwest New Mexico migrated northeastward and southwestward repeatedly across the basin for some 30 million years, as a result of the four to five major transgressions and regressions, depositing about 6,500 ft of marine, coastal plain, and nonmarine sediments mostly during the regression period (Molenaar, 1977; Brian, Price & Editors, 2002). This depositional occurrences were immensely assisted by the rapid subsidence in the San Juan Basin (Huffman Jr., 1987).

Stratigraphy

The Mancos Shale in the San Juan Basin lies between the Dakota Sandstone at the bottom and the Point Lookout Sandstone at the top, and this shale formation can be subdivided into the Lower Mancos Shale and the Upper Mancos Shale (Figure 4). For the purpose of this study, the Upper Mancos Shale will be the main focus. The Upper Mancos Shale lies in between the Juana Lopez Member at the bottom and the Point Lookout Sandstone at the top, and can be found throughout the San Juan Basin, excluding areas with Gallup Sandstone. The Upper and Lower Mancos Shale units are separated by the basal Niobrara unconformity (Dane 1960; Pentilla, 1964; McPeek, 1965; Molenaar, 1973, 1977a; Molenaar and Baird, 1992; Ridgely et al, 2013; Broadhead, 2015). Both of these units display sandy sedimentary deposits and marine mudstone deposits intertonguing.

The Upper Mancos Shale is predominantly dark gray, kerogen-rich marine shale with interbedded marine siltstones and fine-grained sandstones. The shale unit is 900 to 1550 ft thick in the San Juan Basin, and is found to be the thinnest in the southwest, graduating thicker to the northeast in the direction of the basin depocenter.

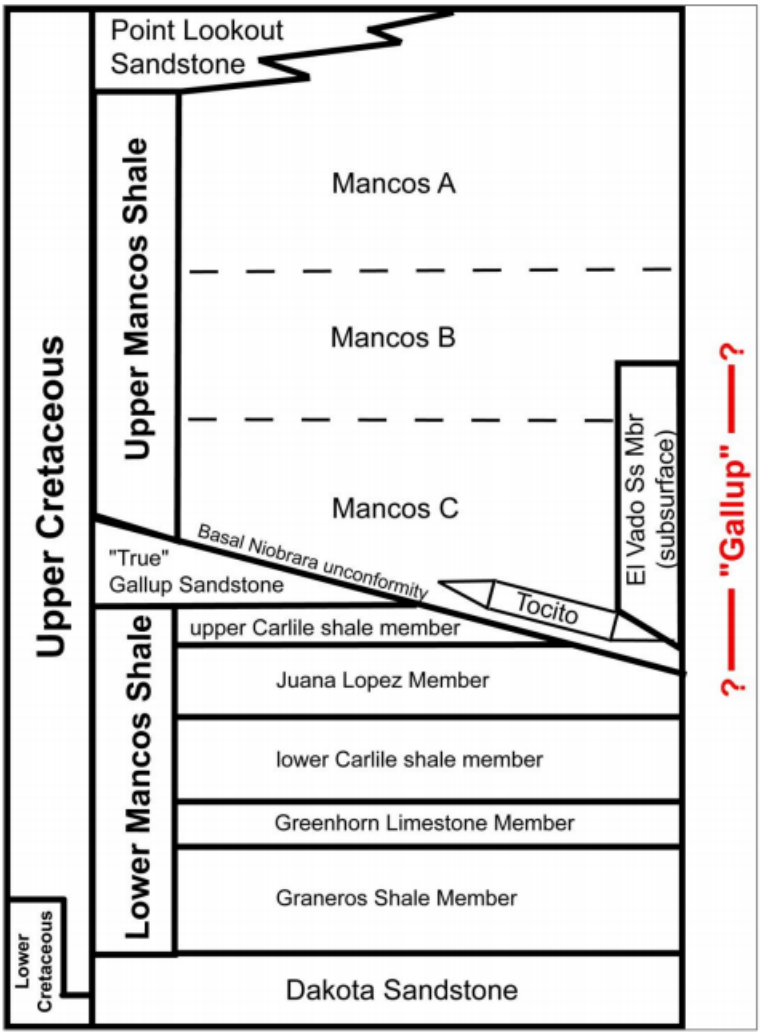

Figure 4. Stratigraphy of the Upper Mancos Shale

Methods

X-Ray Diffraction (XRD)

For the determination of mineralogical abundance through quantitative and qualitative analysis, XRD (X-Ray Diffraction) was performed on all thirteen powdered samples (www.sgs.comm/mining). This test was performed using the Shimadzu MAXima XRD-7000 (Figure 5). The system detects the individual minerals contained in the sample as well as the

percentage of their corresponding weight. Powder sized samples were compacted in the XRD sample holder before calibration, then processed before opening the peak profile spectrum. The minerals were then identified, before generating a model for the minerals. At the end, a pattern deconvolution was carried out, where the changes in the diffracted X-ray intensities were recorded against the sample's rotation angles to derive the XRD pattern (Hu et al., 2019).

Figure 5. Photo of XRD instrument for XRD analyses

Total Organic Carbon (TOC)

The TOC analyses were conducted by GeoMark Research with a Leco C230 instrument (Figure 6). The first step was to decarbonate the rock samples with dilute hydrochloric acid (HCl) by treating the samples for two hours. Then, the samples were placed in a filter for rinsing and flushing by water to remove the acid. The filter was then placed in a Leco crucible to be

dried at 110 °C for at least four hours. Next, the samples were weighed in order to obtain the percent carbonate value based on weight loss.

The samples were combusted in an oxygen atmosphere and any carbon present was converted to carbon dioxide. The sample gas flows into a non-dispersive infrared (NDIR) detection cell. The NDIR measures the mass of carbon dioxide present. The mass was converted to percent carbon based on the dry sample weight. The TOC content is subtracted from the total carbon content to determine the total inorganic carbon content of a given sample.

Figure 6. A Leco C230 instrument for TOC analyses

HAWK Pyrolysis

Pyrolysis is a geochemical analysis method that rapidly yields the information of richness and thermal maturity of potential source rocks. This method was defined by Peters (1986) as the heating of organic matter in the absence of oxygen, to yield organic compounds. The HAWK (Hydrocarbon Analyzer With Kinetics) pyrolysis measures the S1 - free oil (mg HC/g rock), S2 - kerogen yield (mg HC/g rock), S3 - organic carbon dioxide yield (mg CO_2/g rock), and T_{max} - maturity indicator (°C) (Figure 7). The process of this pyrolysis method was achieved by a sequence of controlled heating of the sample under inert gas flow, where the organic matter was pyrolyzed or decomposed in the absence of oxygen. The amount of hydrocarbons were monitored by a flame ionization detector (FID). Lastly the oxidation of the residual rock was recovered after pyrolysis under oxygen. During pyrolysis and oxidation, the carbon monoxide and carbon dioxide released were monitored by an infrared cell. Below were the HAWK operating conditions:

S1: 300°C for 3 minutes

S2: 300°C to 650oC at 25°C /min; hold at 650°C for 0 minute

S3: measured between 300 to 400°C

Figure 7. HAWK instrument for pyrolysis

Besides obtaining S1, S2, S3, and T_{max}, several other useful ratios can be determined from pyrolysis and TOC data. These are:

Hydrogen Index (HI): S2/TOC × 100 (in mg HC/g TOC)

Oxygen Index (OI): S3/TOC × 100 (in mg CO2/g TOC)

Normalized Oil Content: S1/TOC × 100 (in mg HC/g TOC)

Production Index (PI): S1/ (S1+S2)

Calculated %Ro = $0.0180 \times (T_{max} - 7.16)$

Vacuum Saturation

The purpose of this analyses is to investigate the pore structure properties of geological and man-made porous media. This method can also be used to study the edge-only accessible porosity of poorly connected materials, by using differently sized samples.

Before the analyses, three 1 cm^3 cubes from each of the thirteen samples, cubes X, Y, Z, were prepared by saw cutting. These cubes were then oven dried at 60 degree Celsius for 48 hours to remove any moisture in the connected pores of the cubic samples. After the 48-hour period, the cube samples were cooled to room temperature and then were weighed on an analytical balance.

Procedure:

For cubic samples, they were first put into the tray-holder and then placed into the vacuum chamber (Figure 8). After the chamber was properly sealed, the evacuation process started. The first evacuation process removed the air inside the sample for 6 to 8 hours, and the pressure in the chamber would drop to 0.1 torr or less. Then CO_2 was injected into the chamber to replace air inside the sample, as CO_2 is more soluble in water than air. The second evacuation following the CO_2 flushing lasted for around 20 hours. After finishing the second evacuation, de-ionized water (DIW) was added to the vacuum chamber with 30 psi of CO_2 pressure being applied to force water into the samples for 3 to 4 hours. Once the vacuum saturation was complete, samples was taken out of the vacuum chamber. Slightly DIW -moistened napkins were used to wipe off the excess fluid on the sample surface and the saturated weight was recorded in air by an analytical balance. Next, the samples was placed into the Archimedes' bucket (Figure 9) to weigh the submerged weight. The same procedure was used for 2DT (two parts decane and

one part toluene). Finally, the following equations below were used to determine the porosity, bulk density, and grain density:

$$\varphi = Vo/Vb = (Ws-Wd)/Wf$$

$$\rho b = Vo/Wd = (Ws-Wd)/\rho f$$

$$\rho g = \rho b/(1-\varphi)$$

where, φ= porosity, no unit

Vo= void volume, cm^3

Vb= bulk volume, cm^3

Ws= sample weight with fluid saturation, g

Wd= sample over-dry weight, g

Wf= sample submerged weight in fluid, g

ρf= fluid density, g/cm^3

ρb= bulk density, g/cm^3

ρg= grain density, g/cm^3

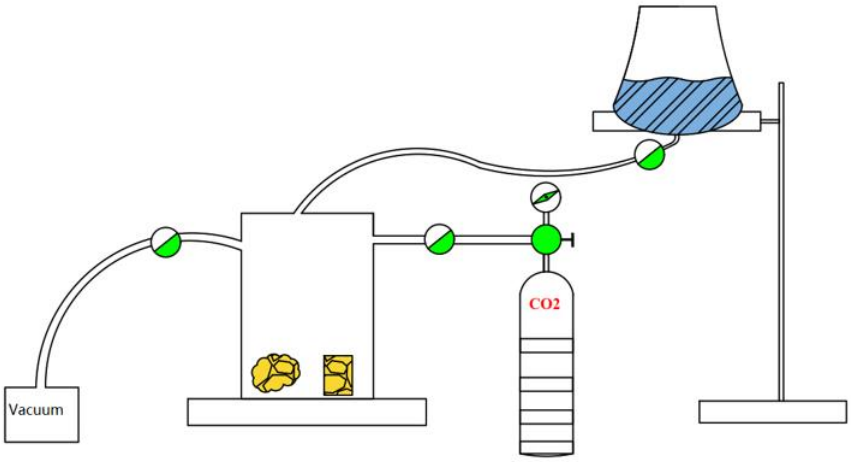

Figure 8. Diagram of vacuum saturation experimental set-up

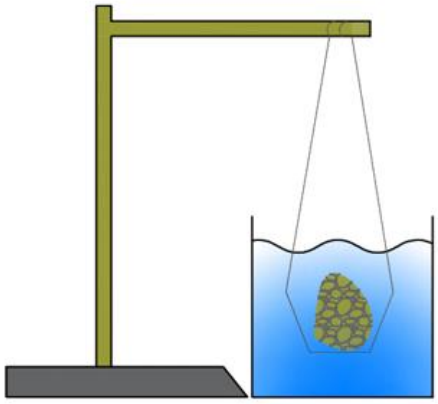

Figure 9. Bucket measurement by the Archimedes' principle

Helium Pycnometry

Sample Preparation:

Cylindrical, cubic, and granular samples were required for grain density and bulk density analyses. The samples were first oven dried for 48 hours at 60 degrees Celsius. Then, they were put into a desiccator to be cooled to room temperature.

Grain Density

Accupyc II 1340 by Micrometrics was used to measuring volume and calculate true or skeletal/apparent density (Figure 10). The instrument uses the ideal gas law equation and the gas displacement technique.

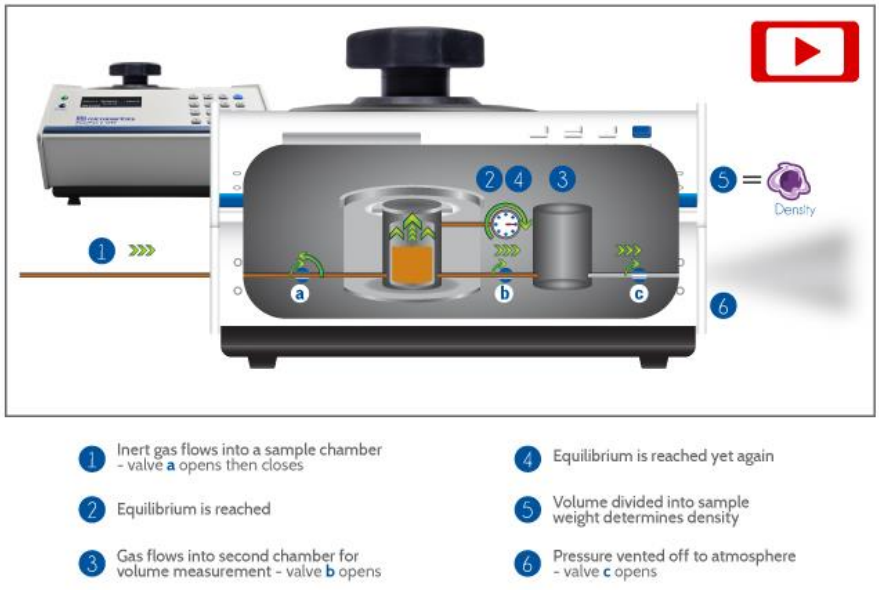

Figure 10. Accupyc II 1340 by Micrometrics for grain density analyses

There are two chambers inside the instrument, which are a sample chamber and an expansion chamber. The sample chamber is pressurized with gas from a helium or nitrogen tank set to 22 pounds per square inch (psi) of pressure. To purge the system, the fill valve is opened

and then the expansion valve is also opened. Then, the gas is vented out of the unit. Before the analysis, the system is purged using this process. The instrument contains analytical routines to allow a programmed purging of the sample chamber, which in this work, is 10 times. By filling the chamber and venting, it does a better job of cleaning the samples than just blowing gas over the sample. The analysis uses the same filling and venting cycle with time allowed for a pressure equilibration. During the analysis, the instrument automatically records the pressure of first the filling chamber and then the filling and expansion chambers p1 and p2. The unit then calculates the volume of gas displaced by the sample, by collecting volume data, and together with the sample mass, to calculate the skeletal density with the following equations:

$V_{sample} = V_{cel} - [V_{exp}/((P_1/P_2)-1)]$

$Density_{Gr} = M_{samp} / Volume_{samp}$

V_{sample} = Volume of Sample (cm^3)

V_{cel} = Volume of empty chamber (cm^3)

P_1 = Pressure in filling chamber (Pa)

P_2 = Pressure in filling and expansion chamber (Pa)

$Density_{Gr}$ = Grain Density (g/cm^3)

M_{samp} = Sample mass (g)

$Volume_{samp}$ = Sample Volume (cm^3)

Bulk Density

Geopyc 1365 was used to measure the bulk density of the porous samples. This unit determines the density and volume a sample by DryFlo displacement, which is a narrow distribution of small, rigid spheres that consist of a high degree of flow ability to achieve close packing around the sample (micromeritics.com). This medium is small enough to wrap closely to the surface of the sample while not invading the pore space of the sample. The technique of this unit is done by a controlled method of compaction (micromeritics.com). The DryFlo is placed into the precision cylinder. Then, a preliminary compaction with only the DryFlo in the cylinder was performed, where a plunger compressed the DryFlo as the cylinder vibrated, to establish a zero-volume baseline (Figures 11-12).

After that, the sample was placed in the cylinder with the DryFlo and the compaction process was repeated (micromeritics.com). "The difference in the distance (h_t) that the piston penetrates the cylinder during the test, and the distance (h_0) it penetrates during the baseline procedure ($h=h_0 - h_t$), is used to calculate the displacement volume of the medium using the formula for the volume of a cylinder of height h, $V = \pi r^2 h$". (micromeritics.com)

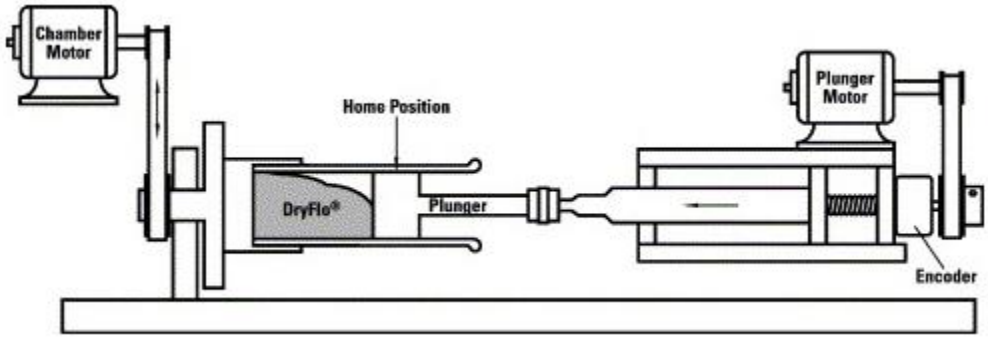

Figure 11. Schematic drawing of GeoPyc instrument (Forsmo and Vuori, 2005)

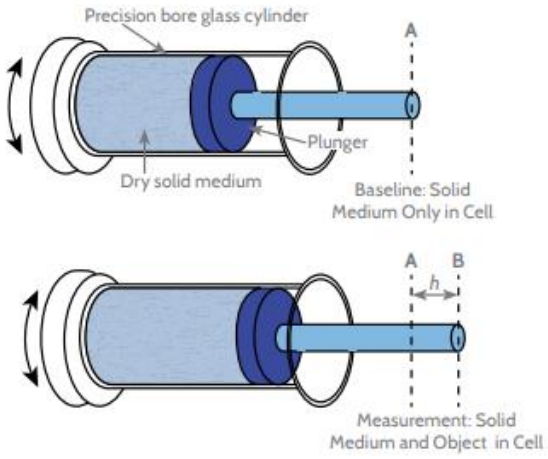

Figure 12. Cylinder with the DryFlo and the compaction process

Low Pressure (N_2) Physisorption

This experiment was conducted with an Accelerated Surface Area and Porosimetry System (ASAP 2460) by Micromeritics (Figure 13). The purpose of this experiment is to determine a sample's surface area and porosity. The sample size of GRI (#20-#35 mesh size) was used for all 13 samples for this experiment. The quantity of nitrogen gas adsorbed onto or desorbed from a solid surface was measured at various equilibrium vapor pressures to quantify the surface area and pore structure of a porous sample (Hu et al., 2019). This was achieved by administering N_2 gas to the sample surface at varying pressures. The method was carried out at a constant temperature of −196.15°C (−321.1°F), controlled by liquid N2, at a relative pressure (P/P_o) in the range 0.001 to slightly less than 1.0 for N_2 gas. The amount of N_2 gas adsorbed by the sample was recorded at each gas the ampressure, resulting in gas adsorption/desorption isotherms. The Barrett-Joyner-Halenda (BJH) and density functional theory (DFT) models were used to obtain pore size distributions. The BJH model measures pore throat widths in the mesopore range (2–50 nm), with the ability to detect a small fraction of macropores (>50 nm)

(Barrett et al., 1951; Wood and Hazra, 2017). The DFT model measures pore throat widths in the micropore (<2 nm) to mesopore range (Neimarka et al., 2009). Used together, both models give a better description of the pore-size distribution of a sample.

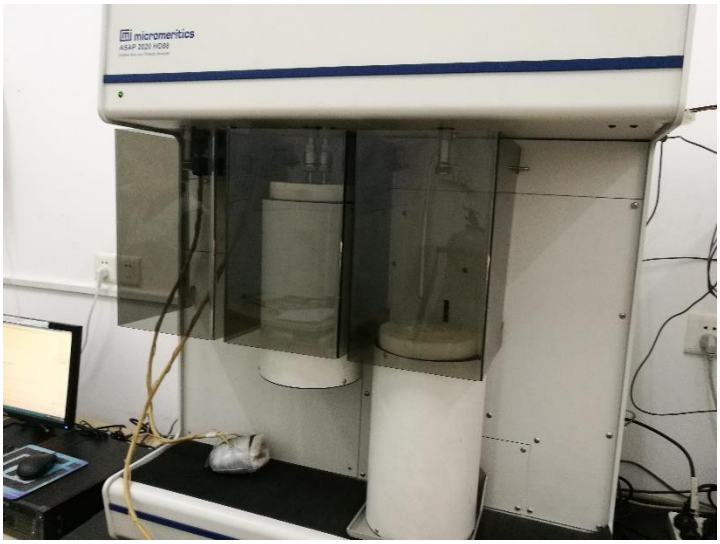

Figure 13. Accelerated Surface Area and Porosimetry System (ASAP 2460) by Micromeritics

Wettability/Contact Angle

According to Lu et al. (2019), "The wettability of shale oil reservoirs is an important petrophysical property to determine subsurface multiphase flow and residual oil saturation". Due to the tremendously low permeability of the shale matrix, a cost-effective method whereby a combination of horizontal drilling and multistage hydraulic fracturing is needed to achieve shale liquid reservoirs' potential (Lu et al., 2019). Contact angle is one of many methods for testing the wettability of a rock sample. Contact angle, θ, is defined as the angle between a tangent of gas-liquid interface and that of solid-liquid interface formed at the three phases' boundary where liquid, vapor and solid intersect.

In this analysis, the SL200KB Optical Dynamic/ Static Interfacial Tensiometer & Contact Angle Meter was used, along with four fluids to determine the wettability characteristics of each sample (Figure 14). The four fluids are DIW (hydrophilic fluid), API (American Petroleum Institute) brine (fluid in reservoirs), 2DT (hydrophobic fluid), and 10% IPA (isopropyl alcohol) (amphiphilic fluid). A drop of each fluid was applied onto the pre-polished surfaces of samples (~1 cm x 1 cm x 0.3 cm) while capturing images of the proceedings simultaneously.

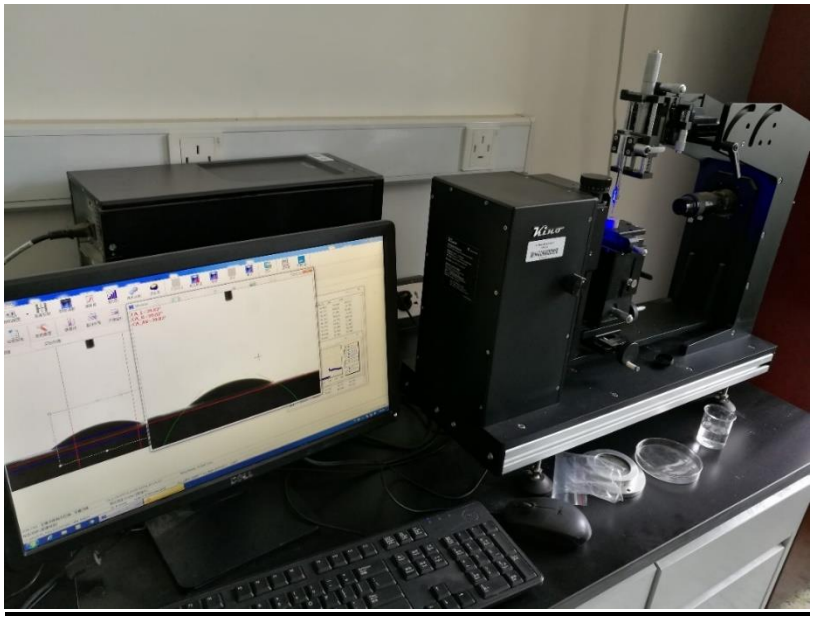

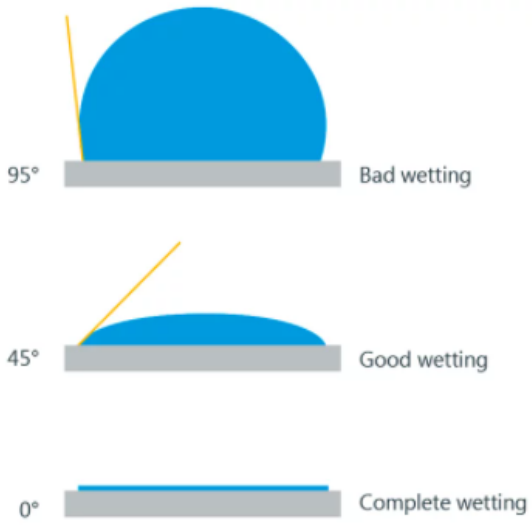

Figure 14. SL200KB Optical Dynamic/ Static Interfacial Tensiometer & Contact Angle Meter (top) and wettability characteristics by contact angle (bottom)

Fluid Imbibition

The purpose of this experiment is to monitor the quantity and rate of liquid imbibed into a porous solid sample (Hu et al., 2001). 1 cm^3 cubes were used for each of 13 samples for this experiment. As part of the preparation for this experiment, each cube was applied with epoxy on all faces except for the top and bottom ones. Then, these cubes were oven-dried at 60 degrees Celsius for 48 hours. After that period, the cubes were then placed into a desiccator to be cooled to room temperature. The procedure of this experiment was as follow (Figure 15):

First, activate the logger software called Pomiar Win, then, weigh out enough liquid solution into a pan for the sample to be immersed and place the pan into the chamber, which have two bottles of water already inside to maintain a high relative humidity. After that, weigh and record the sample weight, the holder weight and sample with the holder weight. Next, turn the knob of the lab jack to raise the chamber until the bottom of the sample is submerged in the liquid at about 1 mm and immediately start logging the data. This experiment ran for a 24 hour and 8 hour period for DIW (hydrophilic fluid) and 4 hour run for 2DT (two parts of decane mixed with one part of toluene) solution (hydrophobic fluid). In order to prevent from collecting unnecessarily large amount of data, log every second for the first 2 minutes, every 30 seconds for 1 hour, every 120 seconds for 6 hours, and every 300 seconds for 24 hours. When the experiment ends, record the balance reading and lower the height of the chamber to remove the sample from the solution. Next, weigh the pan with the remaining solution in, then, weigh a moist Kimwipe tissue paper and record the weights, and then wipe the sample bottom of excess water droplets

and weigh the sample with the holder. After that, weigh the sample by itself and the holder by itself. Below is the mathematical formula for this experiment:

$$Q_w^2 = (2P_c k_w \varphi A_c 2S_w/\mu_f)t$$

Q_w: total volume of water imbibed in (cm^3)

P_c: capillary pressure (Pa)

K_w: the effective permeability of the porous medium to a wetting fluid (cm^2)

A_c: imbibition cross-sectional area (cm^2)

S_w: water saturation (%)

μ_f: fluid viscosity (Pa*s)

φ: sample porosity

t: imbibition time (s)

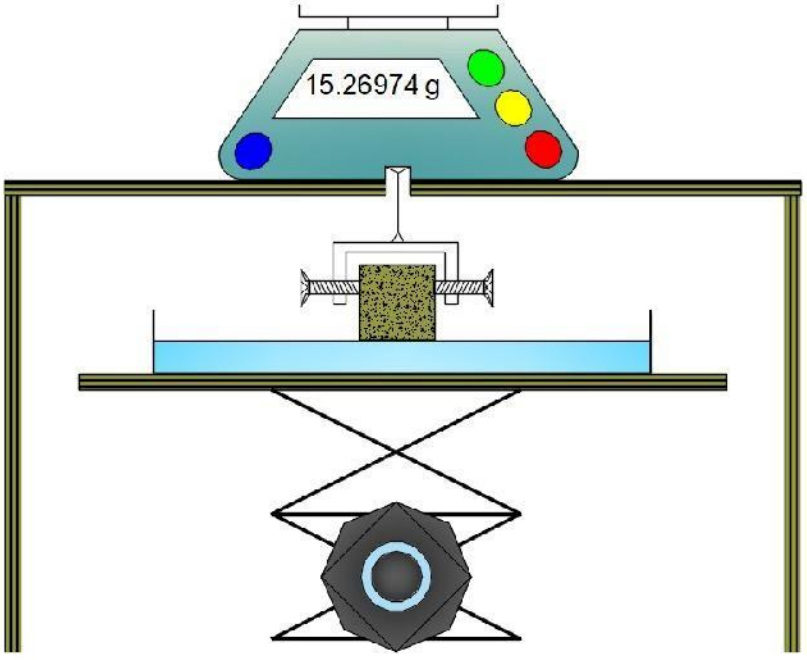

Figure 15. Experimental setup for the fluid imbibition

Results

XRD

This experiment detected five different types of minerals, which are quartz, feldspar, carbonates, sulfides, and clays. Samples from Well Burnham 1 has a range of quartz minerals from 16.4%-21.9%, feldspar from 5.1%-8.4%, carbonates from 24.3%-34.3%, sulfide from 1.2%-1.7%, and clays from 37.8%-47.2%. Well 11x30 has a range of quartz minerals from 21.7%-35.1%, feldspar from 4.8%-18.4%, carbonate from 10.1%-20.2%, sulfide from 1%-1.9%, and clays from 32.4%-60.4%. From the only sample from Well JW2, the results are 30% of quartz, 18.6% of feldspar, 14% of carbonate, 2.2% of sulfide, and 35.2% of clays. Lastly, the Well 148M has a range of quartz minerals from 17.3%-26.9%, feldspar from 5.7%-8.4%, carbonate from 17.1%-31.5%, sulfide from 1.3%-1.5%, and clays from 45.7%-48.9%. The percentages of each of the mineral types are represented by pie charts below for each of the samples from the four wells (Figures 16-18). The average of the types of minerals was used for lithofacies classification, and the result shows that the samples are classified in three different lithofacies-Argillaceous Siliceous Mudstone, Mixed Argillaceous Mudstone, and Mixed Mudstone (Figure 19). The majority of these samples was evenly distributed between Argillaceous Siliceous Mudstone (11x30-1884U, 11x30-1894U, 11x30-1926U, JW-4900M, 148M-6418L, 148M-6476L) and Mixed Mudstone (11x30-1884U, B-4246M, B-4253, B-4256M, 148M-6531L, 148M-6598L) with six samples in each classification. Only one sample (11x30-1915U) falls in the Mixed Argillaceous Mudstone classification.

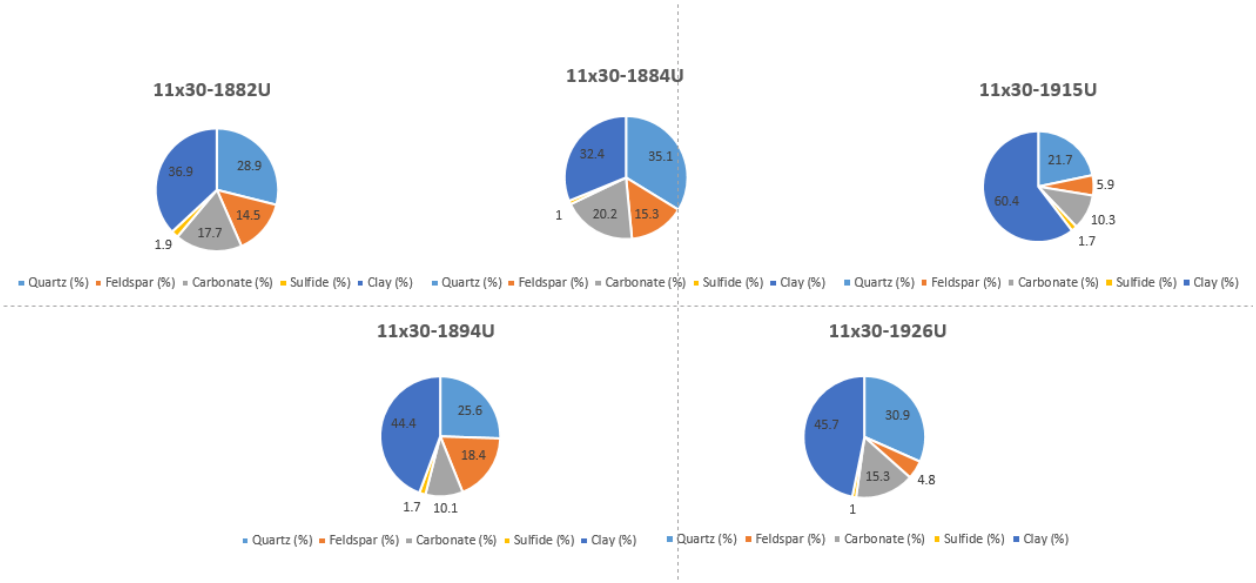

Figure 16. Mineralogy breakdown for samples from Well 11x30

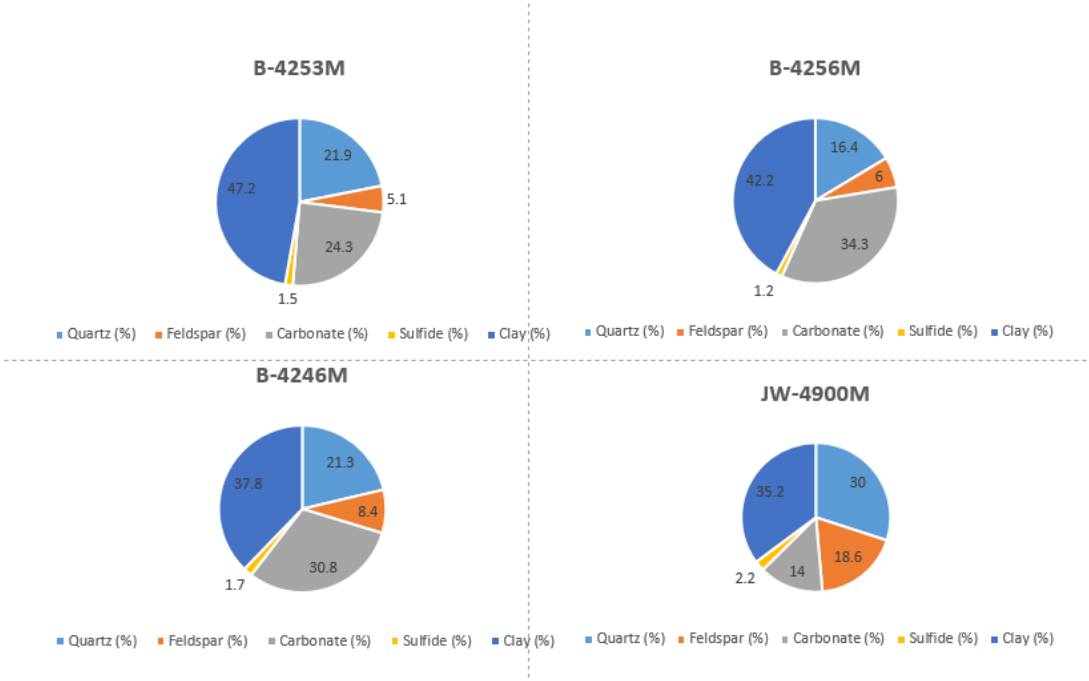

Figure 17. Mineralogy breakdown for samples from Well Burnham 1 and JW2

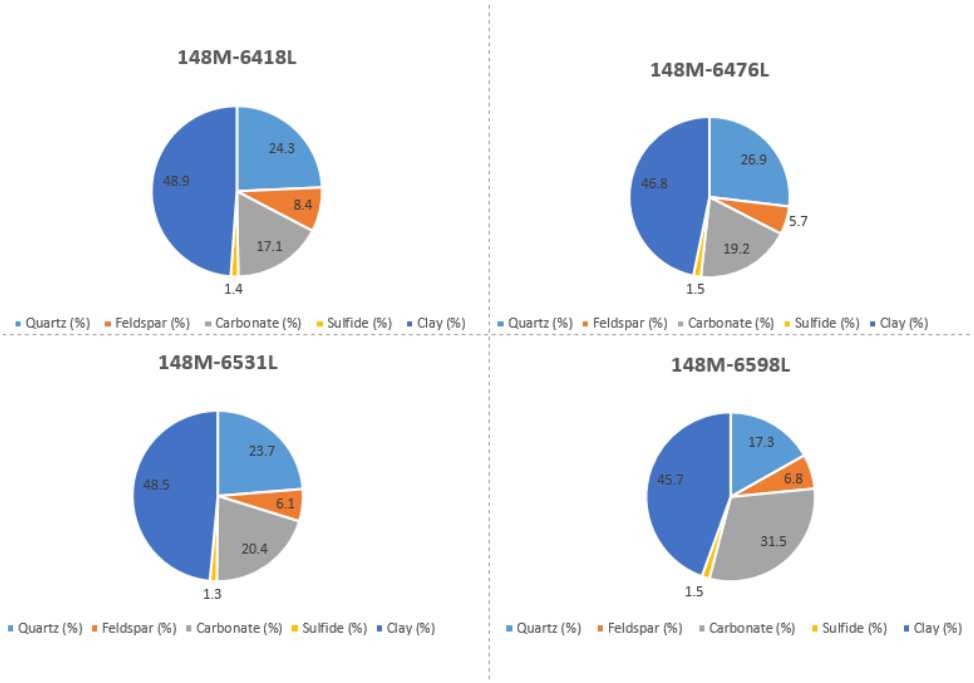

Figure 18. Mineralogy breakdown for samples from Well 148M

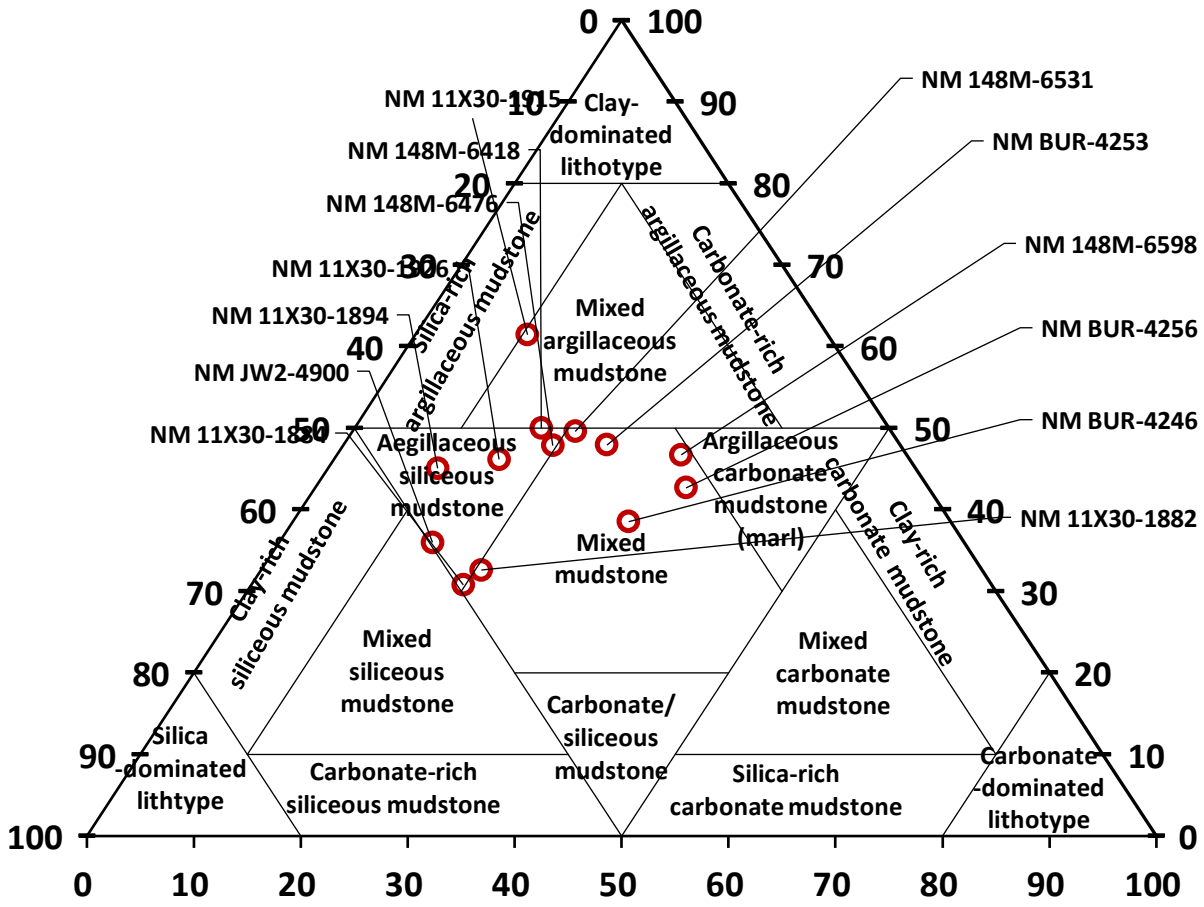

Figure 19. Lithofacies classification of 13 samples used in this study.

TOC

Twelve, from a total of 13, samples were subjected to the TOC analyses. The results from Leco TOC analyses are shown in Table 1 below. TOC is the measure of organic richness (Laughland, 2017) as it represents the quantity of carbon available to form hydrocarbons. From all four wells, the TOC contents range from 0.74% - 2.10%, with the highest TOC value of 2.10% from 148M-6598L and the lowest TOC value is 0.74% from 11x30-1884U. There seemed to be no trend relating TOC values with depth, except for Well 148M, which shows an increase of TOC values from 1.34% to 2.10% at a depth of 6418 ft and 6598 ft respectively.

Rock ID	Leco TOC
	(wt%)
11x30-1882U	1.20
11x30-1884U	0.74
11x30-1894U	1.09
11x30-1915U	1.36
11x30-1926U	0.88
B-4253M	2.01
B-4256M	1.89
JW-4900M	0.78
148M-6418L	1.34
148M-6476L	1.58
148M-6531L	1.61
148M-6598L	2.10

Table 1: Summary of TOC values for each sample.

HAWK Pyrolysis

The HAWK pyrolysis from GeoMark Research yielded S1, S2, S3, and T_{max}, whereas values for calculated Vitrinite Reflectance (RE TMAX), HI, OI, Normalized Oil Content, and PI were obtained by equations previously shown in the Method section. Eight samples were chosen for pyrolysis and the results are presented in Table 2. The pyrolysis results show the quantity, type, and maturity of the source rock. First and foremost, the source rock generative potential could be determined by TOC, S1, and S2 values (Peters, 1986; Peters & Cassa, 1994). Although a good source rock must have a high TOC value, it is not the whole truth. Besides having a high TOC content, a good source rock must have a high hydrogen content and a low oxygen content, where the abundance of hydrogen can associate with carbon to generate more hydrocarbon.

A plot of remaining hydrocarbon potential (S2) vs. TOC shows that the samples are between Oil/Gas Prone (Mixed Type II/III) and Dry Gas Prone windows (Figure 20). The S2 vs. TOC plot shows that two samples (B-4253M and B-4256M) fall in the Oil/Gas Prone window, nine samples (11x30-1882U, 11x30-1884U, 11x30-1894U, 11x30-1915U, 11x30-1926U, JW-

4900M, 148M-6418L, 148M-6476L, 148M-6598L) falls in the Gas Prone window, and one sample (148M-6531L) falls in the Dry Gas Prone window. The Pseudo Van Krevelen plot (Figure 21) shows all samples have a kerogen types ranging from Type I to Type III, with the majority of the samples falling in to Type II and III kerogen.

Another plot of Hydrogen Index (HI) (mg HC/g TOC) vs. T_{max} (°C) shows that the kerogen type and maturity of the chosen samples (Figure 22). This plot indicates that two samples (11x30-1884U, 11x30-1926U) are immature and in the type III kerogen zone, four samples (11x30-1882U, 11x30-1894U, 11x30-1915U, JW-4900M, 148M-6418L, 148M-6531L, 148M-6598L) are in the oil generation zone and in the type III kerogen zone, and two samples (148M-6476L, B-4253M, and B-4256M) are in the oil generation zone and in the type II kerogen zone.

The plot of Production Index (PI) vs. T_{max} (°C) shows levels of kerogen conversion and maturity of the chosen samples (Figure 23). This plot shows that all samples from Well 11x30 are in the oil zone with low level conversion, one sample (148M-6476L) in the Condensate Wet Gas Zone, and the rest of the samples (B-4253M, B-4256M, JW-4900M, 148M-6418L, 148M-6531L, 148M-6598L) are in the oil zone. Table 2 shows a compilation of pyrolysis data.

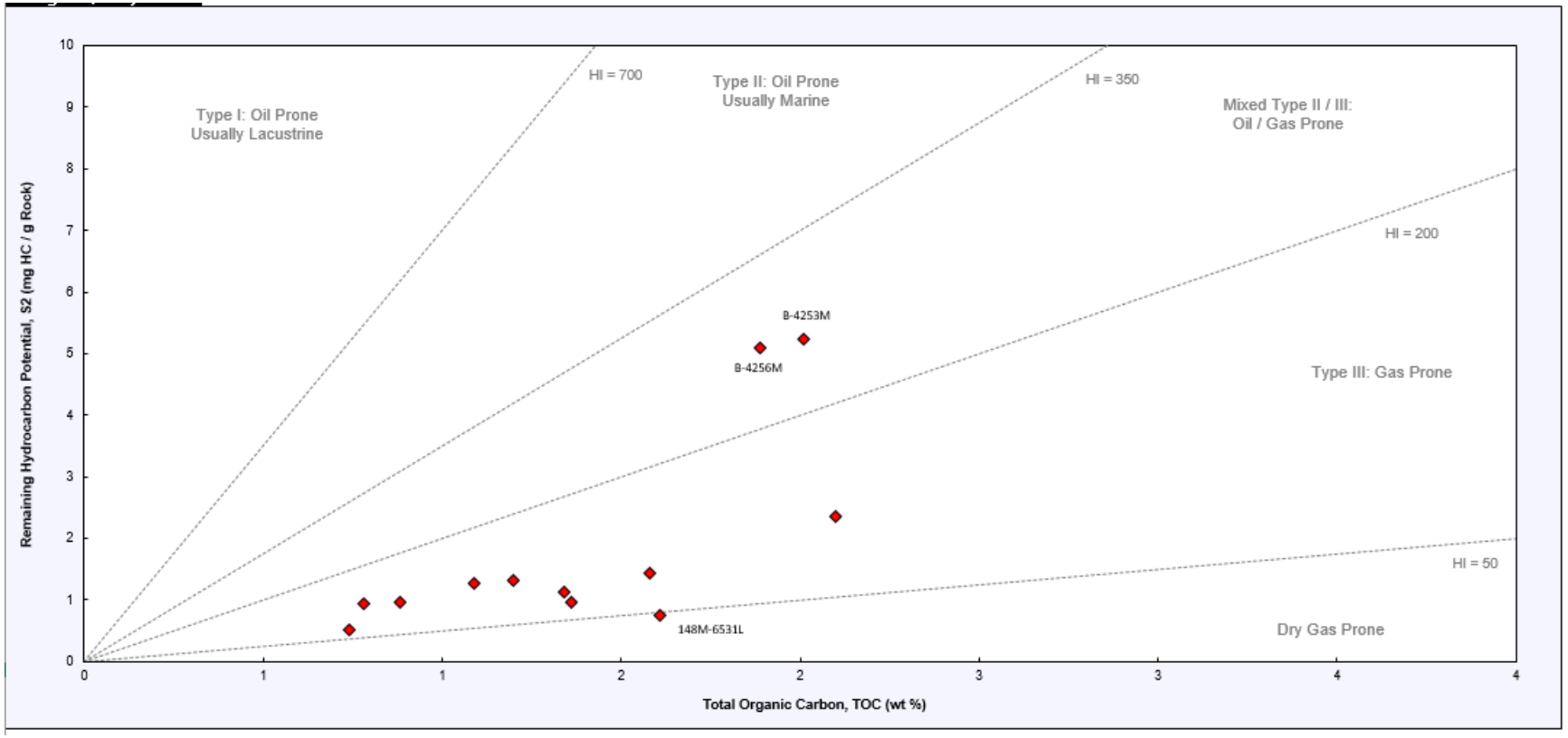

Figure 20. A plot of S2 vs. TOC

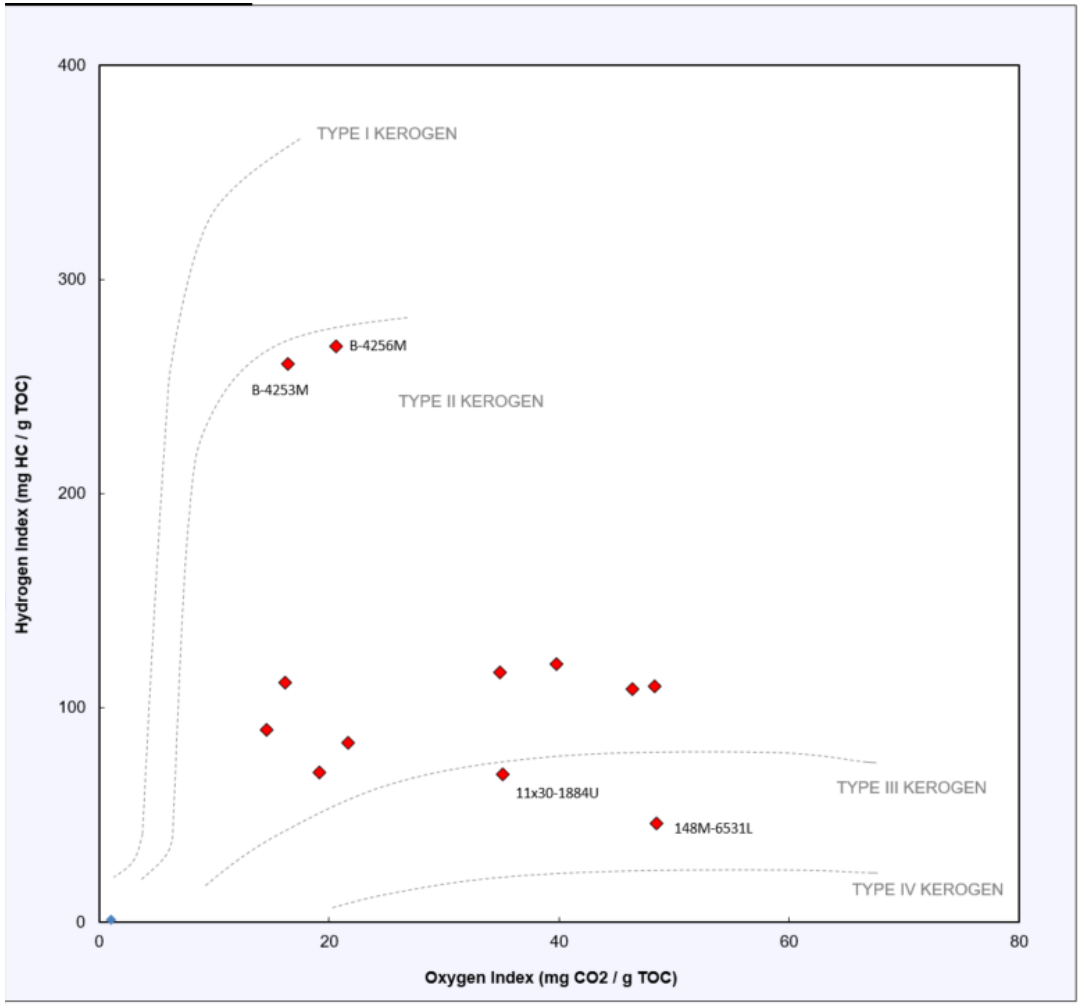

Figure 21. Pseudo Van Krevelen plot of Hydrogen Index vs. Oxygen Index

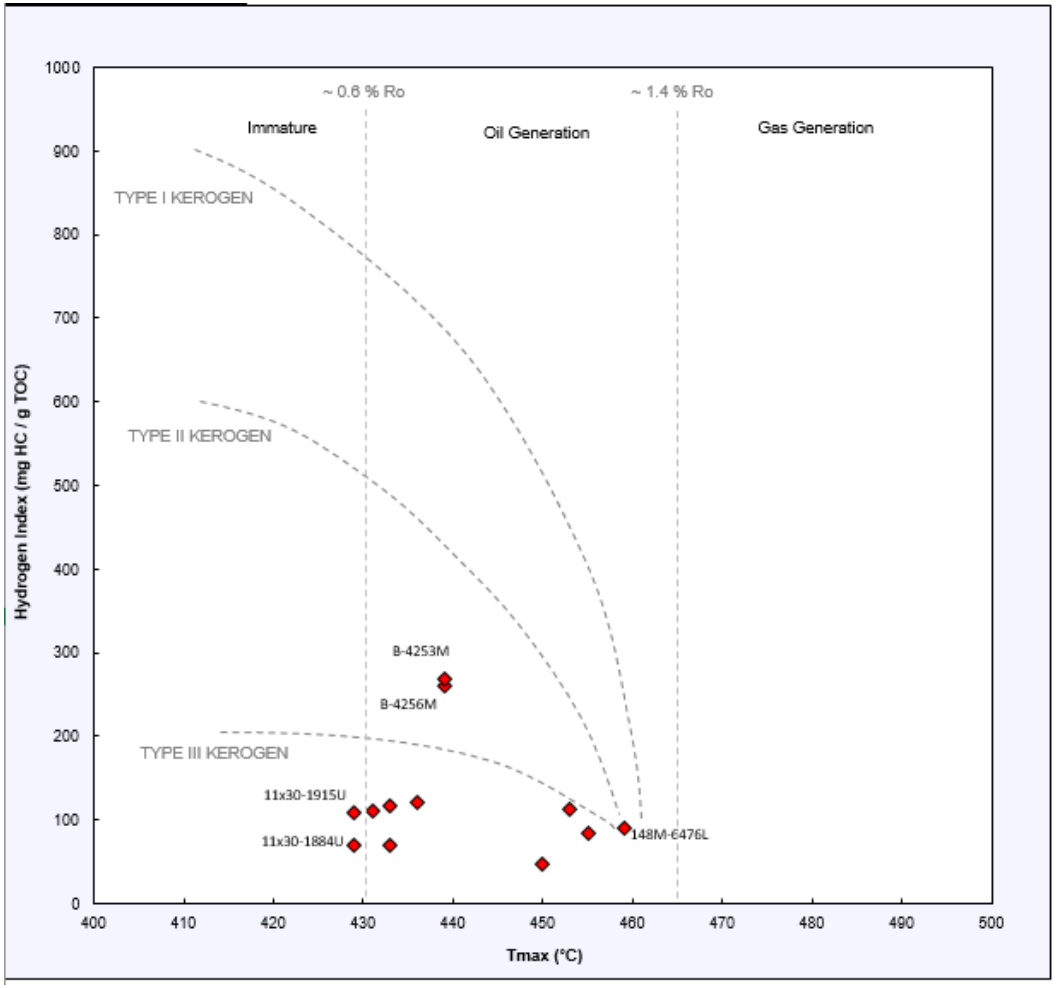

Figure 22. Plot of HI vs. T_{max}

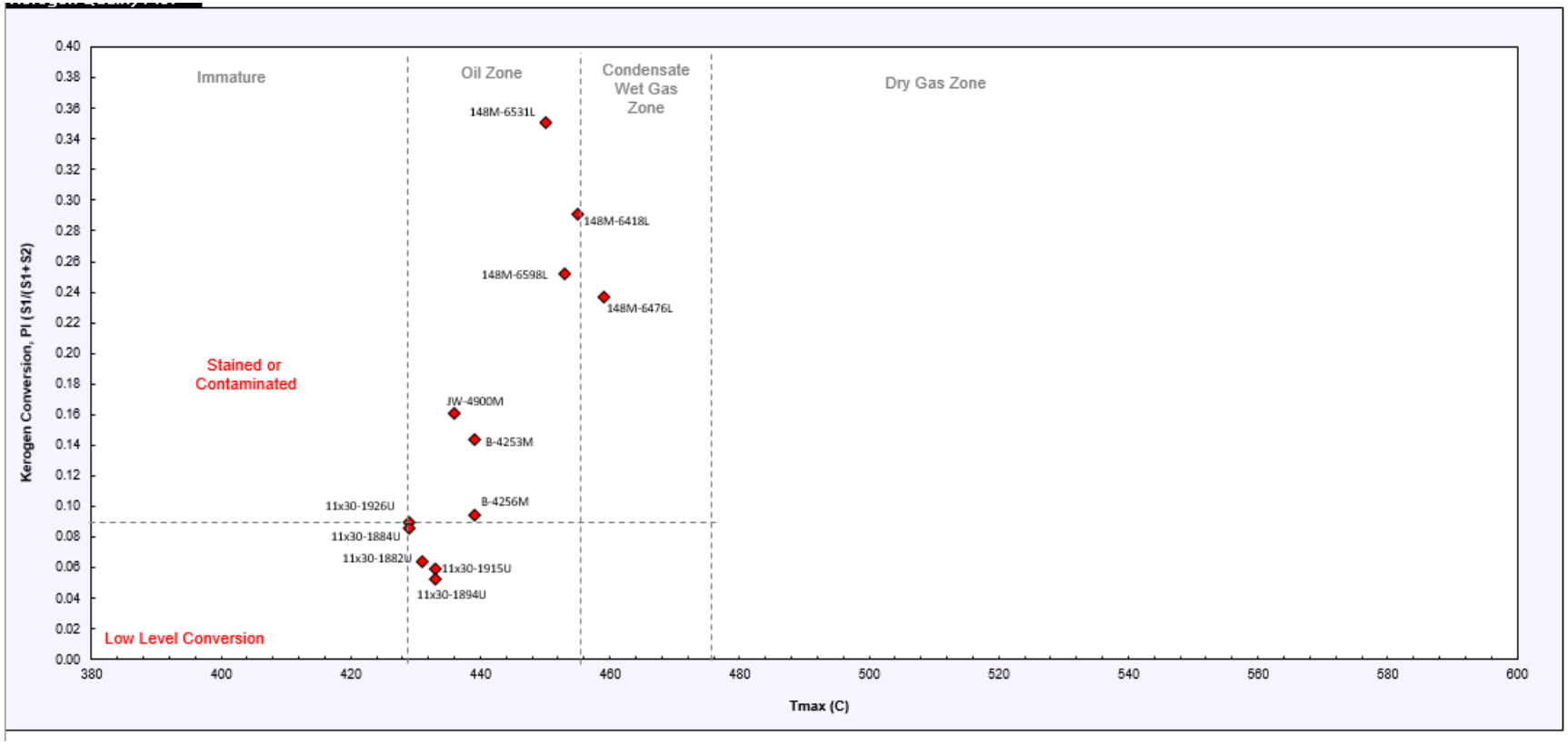

Figure 23. Plot of PI vs. T_{max}.

Rock ID	Well Name	County	State	Depth (ft)	Leco TOC (wt%)	HAWK S1 (mg HC/g)	HAWK S2 (mg HC/g)	HAWK S3 (mg CO2/g)	HAWK Tmax (°C)	Calculated %Ro (RE TMAX)	Hydrogen Index (S2x100/TOC)	Oxygen Index (S3x100/TOC)	S1/TOC Norm. Oil Content	Production Index (S1/(S1+S2)
11x30-1882U	11x30	Mckinley	New Mexico	1,882.00	1.20	0.09	1.32	0.58	431	0.60	110	48	8	0.06
11x30-1884U	11x31	Mckinley	New Mexico	1,884.00	0.74	0.05	0.51	0.26	429	0.56	69	35	7	0.09
11x30-1894U	11x32	Mckinley	New Mexico	1,894.00	1.09	0.07	1.27	0.38	433	0.63	117	35	6	0.05
11x30-1915U	11x33	Mckinley	New Mexico	1,915.00	1.36	0.06	0.95	0.26	433	0.63	70	19	4	0.06
11x30-1926U	11x34	Mckinley	New Mexico	1,926.00	0.88	0.09	0.96	0.41	429	0.56	109	46	10	0.09
B-4253M	Burnham 1	San Juan	New Mexico	4,253.00	2.01	0.88	5.24	0.33	439	0.74	261	16	44	0.14
B-4256M	Burnham 2	San Juan	New Mexico	4,256.00	1.89	0.53	5.08	0.39	439	0.74	269	21	28	0.09
JW-4900M	Joan White 2	San Juan	New Mexico	4,900.00	0.78	0.18	0.94	0.31	436	0.69	121	40	23	0.16
148M-6418L	148M	Rio Arriba	New Mexico	6,418.00	1.34	0.46	1.12	0.29	455	1.03	84	22	34	0.29
148M-6476L	148M	Rio Arriba	New Mexico	6,476.00	1.58	0.44	1.42	0.23	459	1.10	90	15	28	0.24
148M-6531L	148M	Rio Arriba	New Mexico	6,531.00	1.61	0.40	0.74	0.78	450	0.94	46	48	25	0.35
148M-6598L	148M	Rio Arriba	New Mexico	6,598.00	2.10	0.79	2.35	0.34	453	0.99	112	16	38	0.25

Table 2: Result summary from pyrolysis

Vacuum Saturation

This method was used to determine the bulk density, grain density, and porosity of the rock samples. Three 1 cm^3 samples were used for this experiment in both DIW and 2DT liquids with different hydrophobicity. First, the results from the DIW tests yield an average bulk densities of 1.976 to 2.546 g/cm^3, average grain densities of 2.081 to 2.660 g/cm^3, and average porosities of 1.667 to 7.930%. Next, the results from the 2DT tests produce an average bulk density of 2.267 to 2.550 g/cm^3, average grain densities of 2.538 to 2.724 g/cm^3, and average porosities of 3.244 to 13.594%. The compiled summary of the results are shown in Tables 3-4. By comparing the edge-accessible porosities for DIW and 2DT fluids, there seems to have no trend relating to sample depths.

Sample ID	Average Porosity (%)	Average Bulk density (g/cm^3)	Average Grain density (g/cm^3)
11x30-1882U	6.717	2.138	2.290
11x30-1884U	1.667	2.546	2.613
11x30-1894U	5.157	1.993	2.104
11x30-1915U	5.617	2.304	2.446
11x30-1926U	7.930	2.300	2.501
B-4246M	5.103	1.976	2.085
B4253M	5.374	2.281	2.415
B-4256M	5.379	2.184	2.311
JW-4900M	6.080	2.416	2.577
148M-6418L	7.789	2.035	2.207
148M-6476L	7.417	2.536	2.737
148M-6531L	4.820	2.272	2.391
148M-6598L	5.227	2.475	2.614

Table 3. Vacuum saturation results with DIW.

Sample ID	Average Porosity (%)	Average Bulk Density (g/cm3)	Average Grain density (g/cm^3)
11x30-1882U	12.469	2.307	2.635

11x30-1884U	13.594	2.267	2.635
11x30-1894U	11.310	2.346	2.645
11x30-1915U	12.696	2.382	2.729
11x30-1926U	13.245	2.372	2.734
B-4246M	-	-	-
B4253M	4.054	2.435	2.538
B-4256M	3.244	2.473	2.556
JW-4900M	7.137	2.530	2.724
148M-6418L	6.303	2.550	2.722
148M-6476L	4.145	2.541	2.654
148M-6531L	6.274	2.436	2.599
148M-6598L	-	-	-

-: not available

Table 4. Vacuum saturation results with 2DT.

Helium Pycnometry Grain Density

The results for sample sizes ranging from cylinder to powder are shown in Table 5. Generally, the results show a slight trend of increasing grain density with decreasing sample sizes, and it does not show an increase of grain density with depth.

Density (g/cm^3) / Sample ID	Cylinder (2.54 cm dia. 2.60 long)	Cube (1 cm side)	Mesh 8 mm/-8 (X)	Mesh - 8/+12 (GRI+)	Mesh - 12/+20 (A)	Mesh - 20/+35 (GRI)	Mesh - 35/+80 (B)	Mesh - 80/+200 (C)	Mesh - 200 (Powder)	Average
11x30-1882U	2.675	2.631	2.660	2.654	2.673	2.704	2.732	2.769	2.877	2.708
11x30-1884U	2.653	2.645	2.649	2.643	2.646	2.651	2.677	2.694	2.741	2.667
11x30-1894U	2.601	2.605	2.612	2.615	2.630	2.631	2.644	2.647	2.646	2.626
11x30-1915U	2.661	2.617	2.632	2.634	2.635	2.641	2.646	2.645	2.661	2.641
11x30-1926U	2.688	2.632	2.633	2.651	2.651	2.664	2.659	2.673	2.688	2.660
B-4246M	2.602	2.602	2.595	2.602	2.606	2.610	2.621	2.648	2.640	2.614
B-4253M	2.606	2.608	2.611	2.626	2.628	2.632	2.633	2.632	2.653	2.626
B-4256M	2.637	2.610	2.602	2.614	2.634	2.636	2.643	2.658	2.647	2.631
JW-4900M	2.736	2.648	2.646	2.657	2.650	2.661	2.662	2.667	2.673	2.667
148M-6418L	2.736	2.639	2.642	2.644	2.664	2.672	2.669	2.676	2.757	2.678
148M-6476L	2.660	2.637	2.651	2.672	2.676	2.693	2.693	2.697	2.745	2.680
148M-6531L	2.736	2.634	2.672	2.688	2.676	2.666	2.681	2.710	2.748	2.690
148M-6598L	2.611	2.604	2.609	2.607	2.606	2.607	2.613	2.624	2.630	2.612

Table 5. Grain density results (g/cm^3) for different sample sizes.

The DryFlo Enveloping Bulk Density

The summary of the results for bulk density is shown in Table 6. Besides the cylinder size samples, the other sample sizes demonstrate a decrease in bulk density as sample sizes decrease. In comparison to the grain density results, the bulk density measurement has a more consistent trend of decreasing bulk density as the sample size decreases.

Density (g/cm^3) / Sample ID	Cylinder (2.54 cm dia. 2.60 long)	Cube (1 cm side)	Mesh 8 mm/-8 (X)	Mesh - 8/+12 (GRI+)	Mesh - 12/+20 (A)	Mesh - 20/+35 (GRI)	Mesh - 35/+80 (B)	Mesh - 80/+200 (C)	Average
11x30-1882U	2.374	2.514	2.439	2.391	2.320	2.051	1.703	1.248	2.130
11x30-1884U	2.366	2.637	2.408	2.352	2.074	1.966	1.683	1.240	2.091
11x30-1894U	2.409	2.764	2.229	2.190	2.165	2.120	1.835	1.266	2.122
11x30-1915U	3.024	2.681	2.432	2.289	2.180	2.107	1.927	1.307	2.243
11x30-1926U	2.849	2.505	2.457	2.345	2.222	2.104	1.817	1.264	2.195
B-4246M	2.648	2.660	2.612	2.611	2.534	2.197	1.905	1.212	2.297
B-4253M	2.591	2.662	2.640	2.615	2.532	2.214	1.924	1.244	2.303
B-4256M	2.748	2.666	2.651	2.642	2.603	2.424	1.952	1.430	2.389
JW-4900M	2.648	2.660	2.612	2.611	2.534	2.197	1.905	1.212	2.297
148M-6418L	3.175	2.790	2.740	2.668	2.294	2.295	1.842	1.325	2.391
148M-6476L	2.631	2.683	2.681	2.658	2.470	2.355	1.942	1.342	2.345
148M-6531L	2.643	2.733	2.724	2.676	2.513	2.295	1.939	1.290	2.352
148M-6598L	2.630	2.590	2.516	2.481	2.367	2.327	2.274	1.729	2.364

Table 6. Grain density results (g/cm^3) for different sample sizes.

Low Pressure (N_2) Physisorption

Based on the classification of Sing (1985), all the isotherms of the samples display Type II shape, which was developed by the International Union of Pure and Applied Chemistry (IUPAC). According to Sing (1985), the Type II isotherm is the normal form of isotherm that corresponds to a non-porous or macroporous (> 50 nm pore diameters) samples. From the adsorption curve, the rounded knee indicates the location of monolayer formation (Figures 24-26). The point where the curve begins to be linear is the changeover point from monolayer to multilayer adsorption. The low slope region of the adsorption curve indicates the first several multilayers. However, it can be seen from the desorption curve that they show a H3 hysteresis loop, which is associated with loose assemblages of plate-like particles forming silt-like pores or mesopores (2~50 nm) (Sing et.al, 1985). So, it is clear that these samples contain both macropores and mesopores.

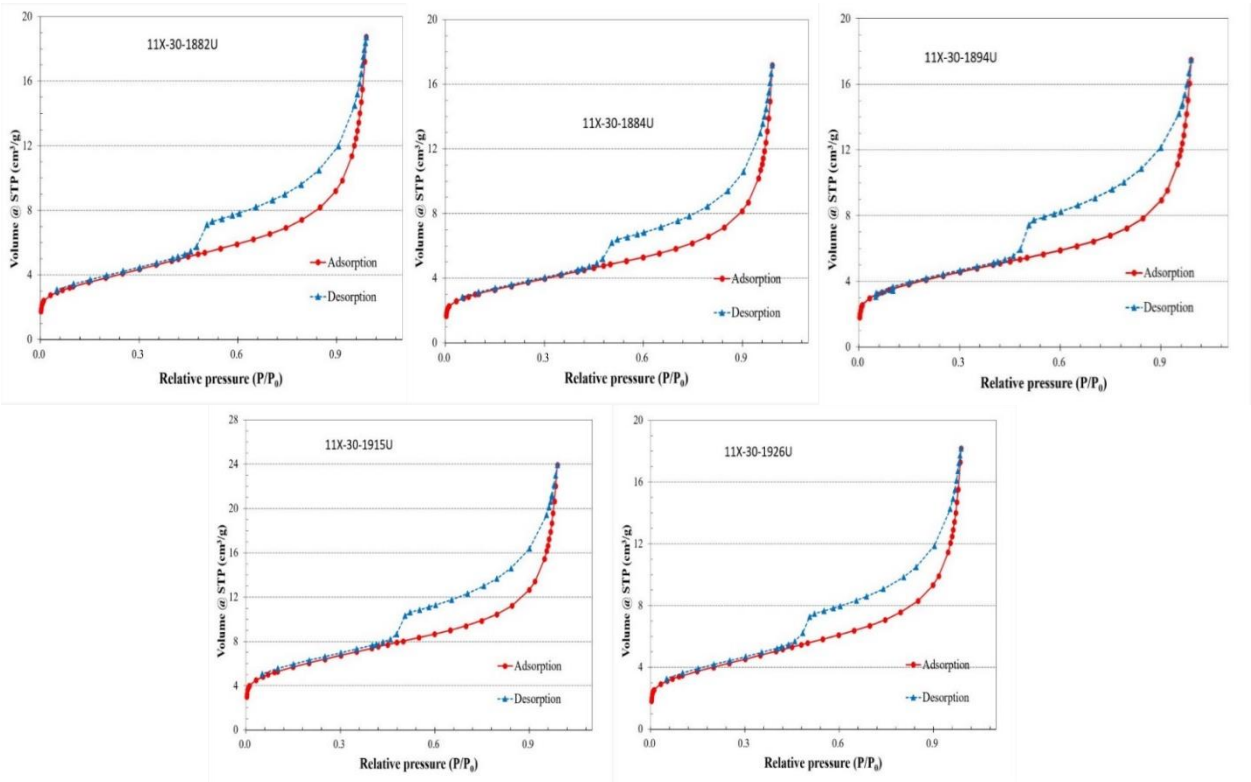

Figure 24.The isotherm for the samples from Well 11x30 which are type II shape and the desorption curve demonstrates a H3 hysteresis loop

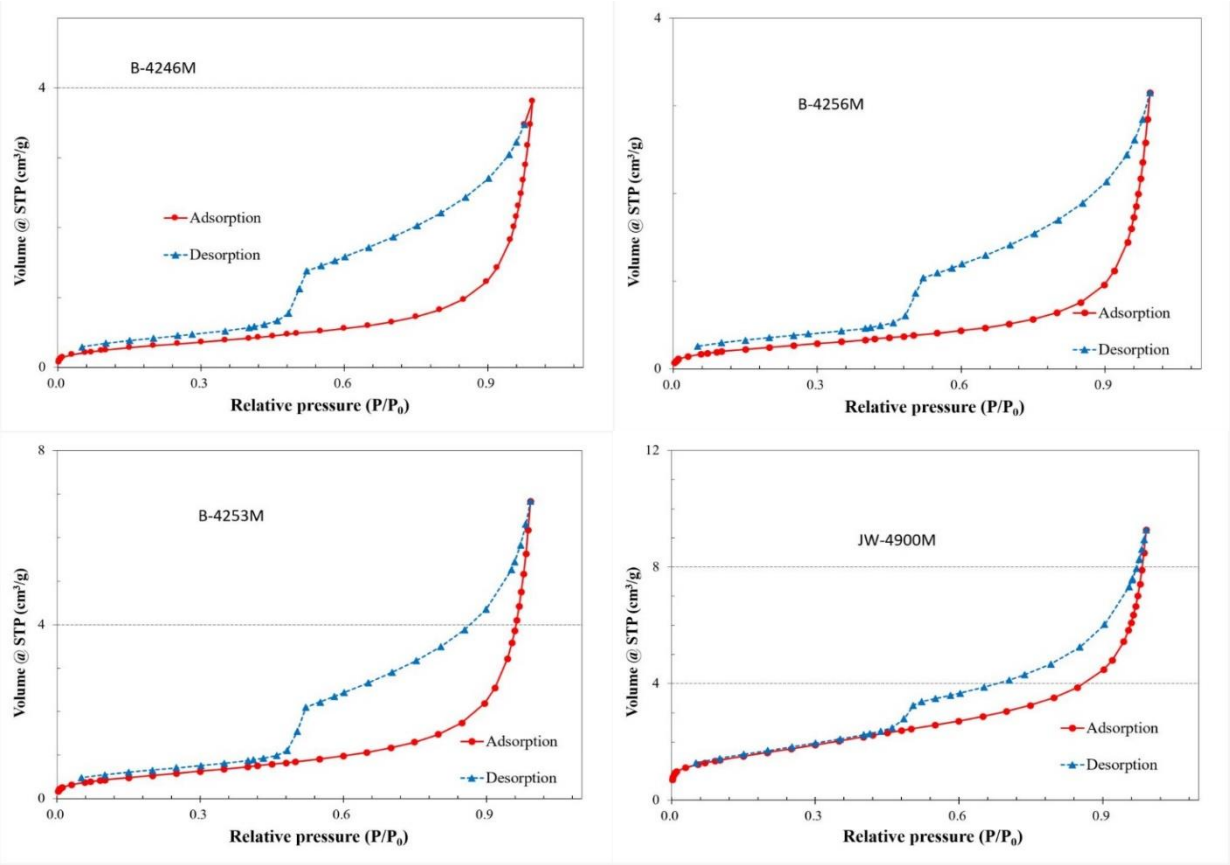

Figure 25.The isotherm for the samples from Well Burnham 1 and JW2, which are type II shape and the desorption curve demonstrates a H3 hysteresis loop

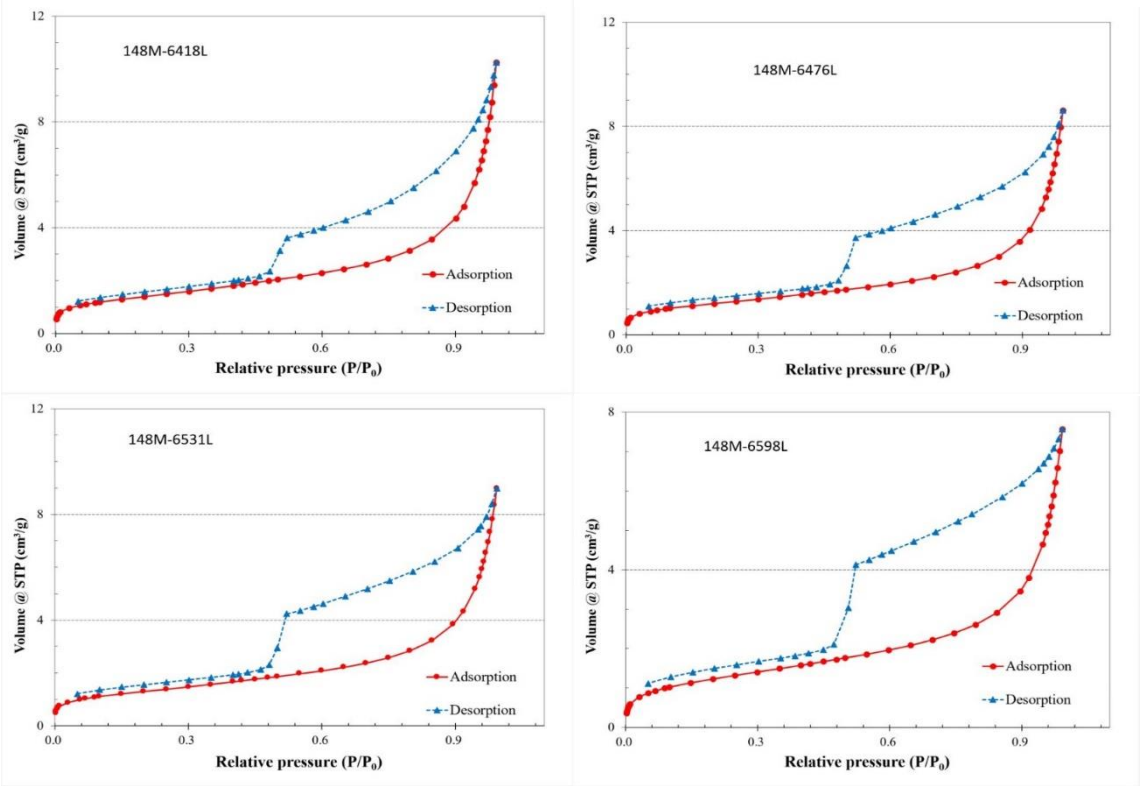

Figure 26.The isotherm for the samples from Well 148M, which are type II shape and the desorption curve demonstrates a H3 hysteresis loop

Next are the curves for the Density Functional Theory (DFT) method for low-pressure gas physisorption tests (Figures 27-29). The graph compares the cumulative pore volume and differential pore volume vs. pore width. The blue curve represents the “Cumulative Pore Volume (V)” and the red curve represents the “Incremental Pore Volume (dV)”. The spikes from the incremental pore volume curve represent the most dominant pore widths.

For Well 11x30, Sample 1882 has a peak at 1.269 nm and higher peaks in the range of 40.03 nm to 93.13 nm; Sample 1884 has a peak at 1.179 nm and higher peaks in the range of 40.03 nm to 86.25 nm; Sample 1894 has the highest peak at 1.269 nm and peaks ranging from 27.27 nm to 86.25 nm; Sample 1915 has the highest peak at 1.179 nm and peaks ranging from

27.27 nm to 86.25 nm; and Sample 1926 has peak at 1.269 nm and higher peaks ranging from 40.03 nm to 93.13 nm.

For Well Burnham 1, there are peaks ranging from 27.27 nm to 68.50 nm, with the highest peak at 40.03 nm for Sample 4246; Sample 4253 also has peaks ranging from 27.27 nm to 68.50 nm, with the highest peak at 40.03 nm; Sample 4256 also have peaks ranging from 27.27 nm to 68.50 nm, but with the highest peak at 37.06 nm. For Well Joan White 2, the only Sample, 4900 has peaks ranging from 27.27 nm to 93.13 nm, with the highest peak at 68.50 nm.

For Well 148M, Sample 6418 has peaks ranging from 25.25 nm 54.42 nm, with the highest peak at 34.33 nm; Sample 6476 has peaks from 25.25 nm to 50.40 nm, with the highest peak at 37.06 nm; Sample 6531 has peaks from 27.27 nm to 40.03 nm, with the highest peak at 34.33 nm; and Sample 6598 has peaks from 27.27 nm to 50.40 nm, with the highest peak at 34.33 nm.

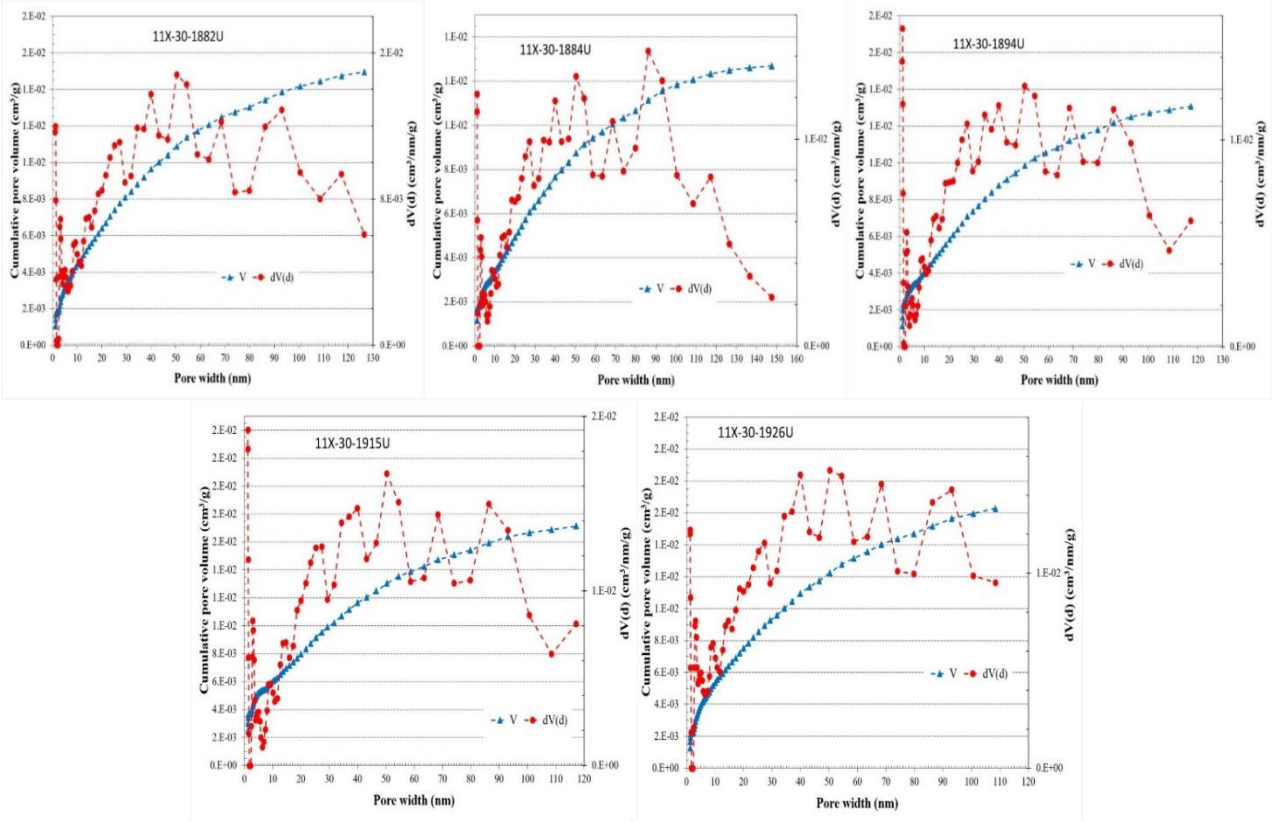

Figure 27. Density Functional Theory (DFT) method's cumulative pore volume and differential pore volume vs. pore width for Well 11x30

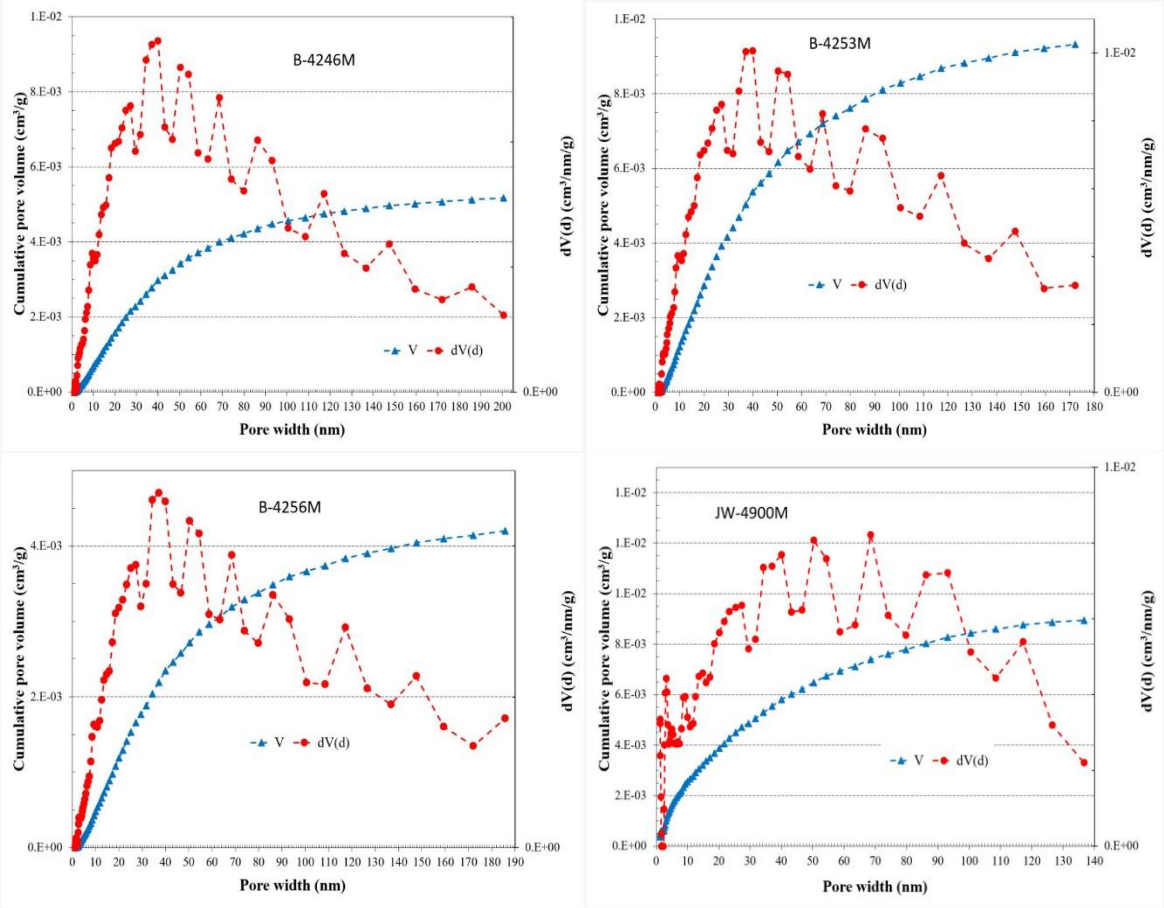

Figure 28. Density Functional Theory (DFT) method's cumulative pore volume and differential pore volume vs. pore width for Burnham 1

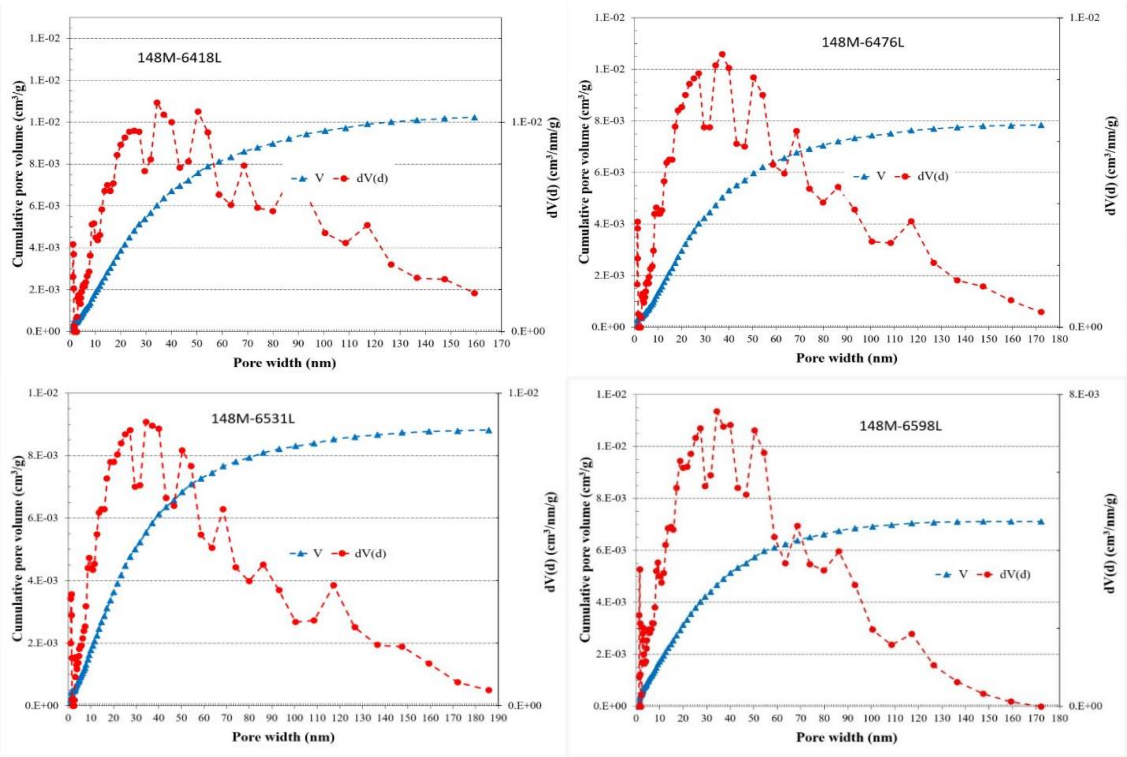

Figure 29. Density Functional Theory (DFT) method's cumulative pore volume and differential pore volume vs. pore width for Well 148M

Contact Angle/Wettability

Figures 30-32 show the final results for contact angle (degrees) of the four fluids plotted against log time (sec). The contact angle results are presented in Table 7 and it shows the data of contact angle at 30 seconds for DIW, API brine, and 10% IPA, while the data for 2DT is at 1 second as the spreading of 2DT on the surfaces of the samples are instantaneous.

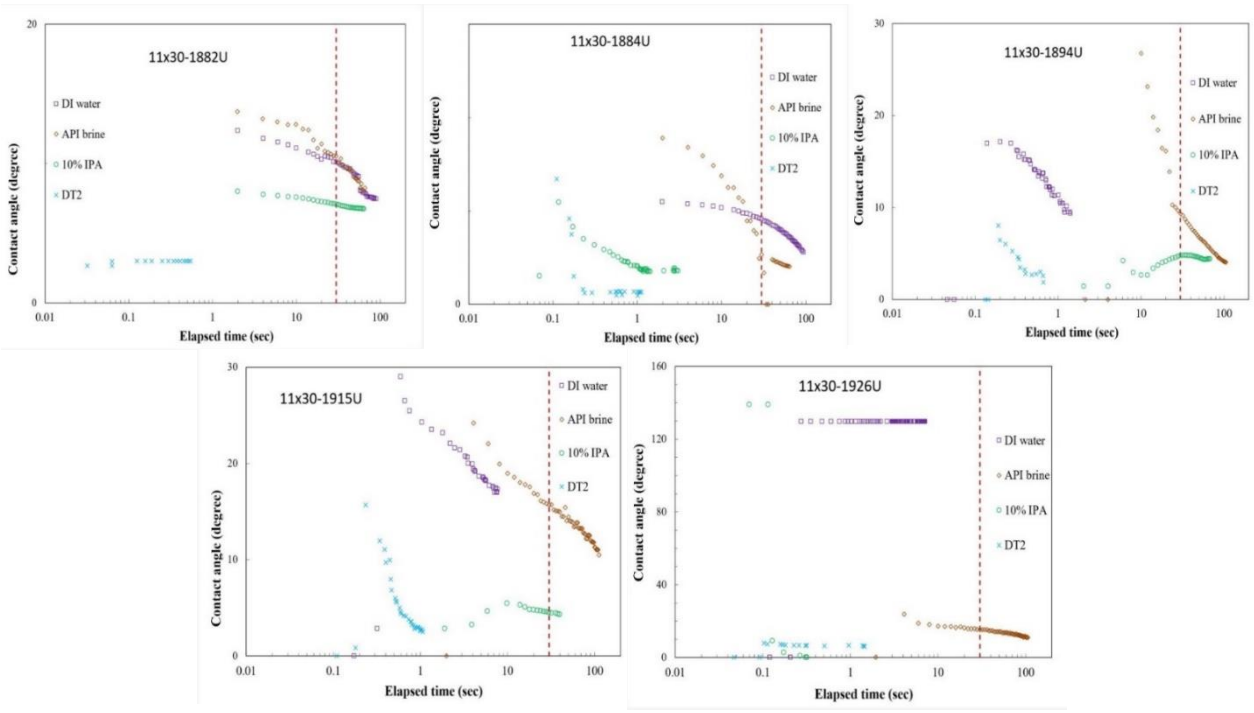

Figure 30. Contact angle (degrees) of the four fluids plotted against log time (sec) for Well 11x30 samples

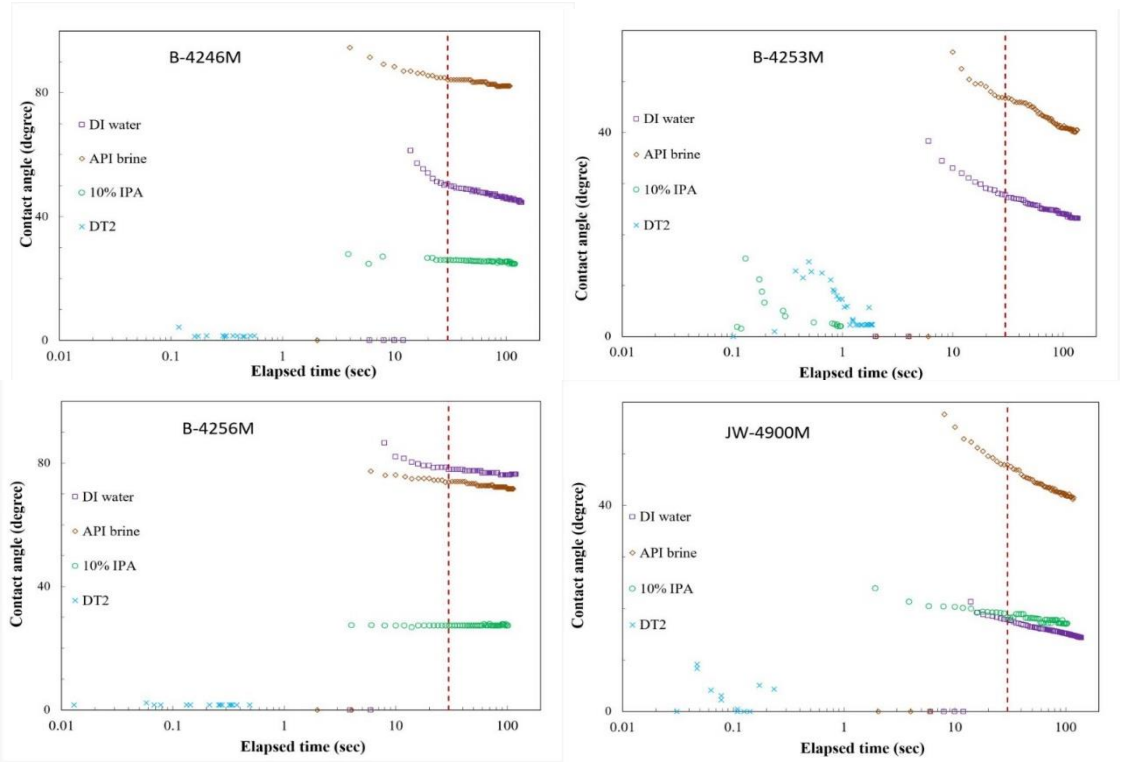

Figure 31. Contact angle (degrees) of the four fluids plotted against log time (sec) for Well 11x30 samples

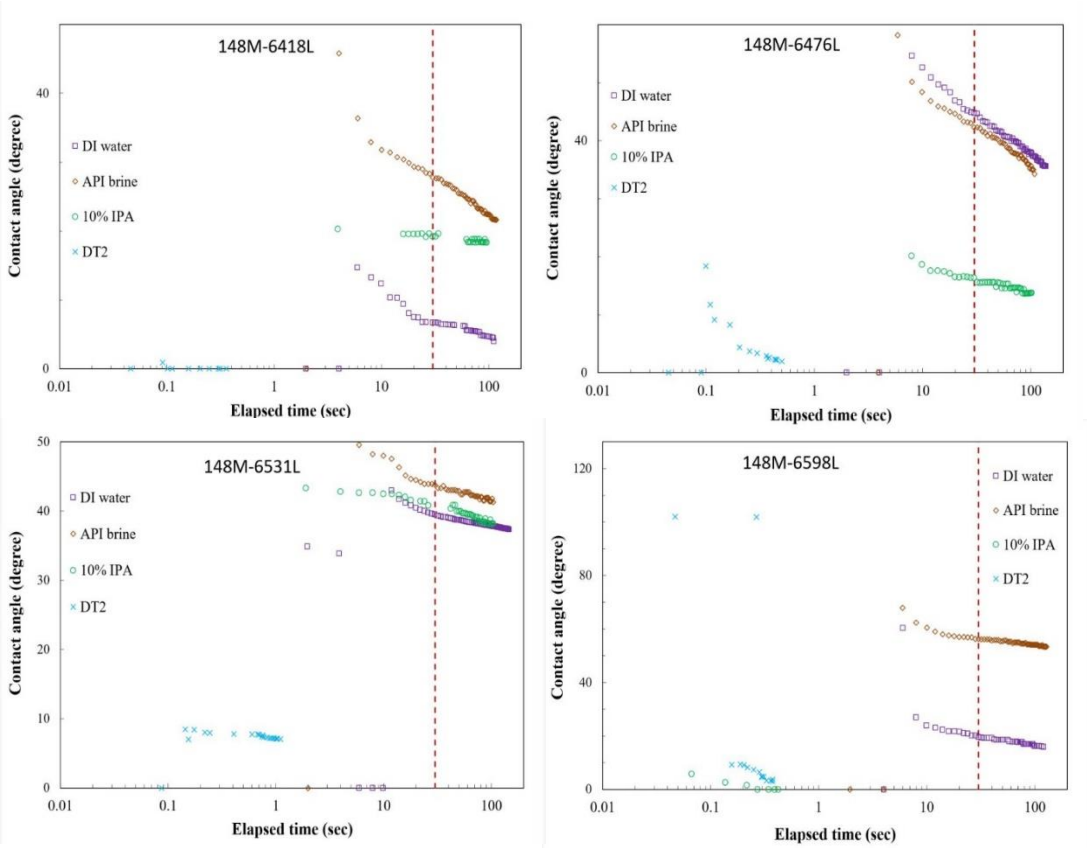

Figure 32. Contact angle (degrees) of the four fluids plotted against log time (sec) for Well 148 samples

Sample ID	DIW (°)	API Brine (°)	10% IPA (°)	2DT (°)
	After 30 seconds			After 1 second
11x30-1882U	10.116	10.530	7.096	-
11x30-1884U	9.128	5.310	-	1.345
11x30-1894U	-	9.328	4.745	-
11x30-1915U	-	15.720	4.538	2.618
11x30-1926U	-	15.250	-	6.559
B-4246M	50.524	84.188	25.948	-
B-4253M	27.762	46.722	-	7.356
B-4256M	77.948	73.765	27.326	-
JW-4900M	17.775	47.852	18.294	-
148M-6418L	6.723	27.780	19.213	-
148M-6476L	44.760	42.292	16.370	-
148M-6531L	39.513	43.789	40.804	7.145
148M-6598L	19.605	56.361	-	-

Table 7. Compilation of results for contact angles of DIW, API brine, 2DT, and 10% isopropyl alcohol (IPA)

DIW, API brine, 2DT, and 10% isopropyl alcohol (IPA) were used to determine the contact angles of different fluids. The DI water represents hydrophilic fluid, and 2DT represents hydrophobic fluid. The 10% IPA is an example of amphiphilic fluid. The API brine is used to mimic fluid in reservoir condition. Based on the results, the contact angle ranges from 6.723° - 84.188° and according to the classification, 0°–10° is considered strong water wet, 10°–70° moderately strong, 70°–110° neutral, 110°– 150° weak, and 150°–180° non-wetting. By using the average of all the results with fluids of DIW, API, and IPA, it is suggested that the Mancos Shale samples are moderately strongly water wet. Besides that, the results with 2DT show that the samples are oil wet due to how quickly the fluid and rock interaction fell below detection limit, which took only 1 second.

Fluid Imbibition

For this experiment, DIW and 2DT solution were used to test the effectiveness of pore connectivity within each rock sample. The behavior of pore connectivity is represented in a curve "Log Cumulative Imbibition (mm)" vs. "Log Time (min)", where the curve is divided into four stages. Stage one is when the sample touches the fluid in the reservoir, where the outer layer of the sample, such as microfractures, lamination, and edge, has contact with the liquid. Stage two represents the fluid imbibed into the wall and edge of the sample. Stage three represents the migration of the fluid into the interior of the sample matrix, and the slope seen in the stage is also called the connectivity slope. Finally, in stage four, the fluid has migrated to the top of the sample and the curve at this stage usually plateau in a stable manner because no more fluid is being imbibed into the sample.

According to Hu et al. (2012), there is a method to classify the connectivity of a sample by looking at its interior stage slope/ connectivity slope. When the slope is 0.5 or larger, the sample is considered to have a high connectivity to the imbibing fluid. When the slope is between 0.26 and 0.5, the sample is considered to have intermediate connectivity. When the slope is 0.26 or lower, the sample is considered to have low connectivity. Figure 33-45 shows the imbibition curves for DIW at 24 hrs testing duration, DIW at 8 hrs, and 2DT at 4 hrs for all samples and the compilation of imbibition data is shown in Tables 8-9.

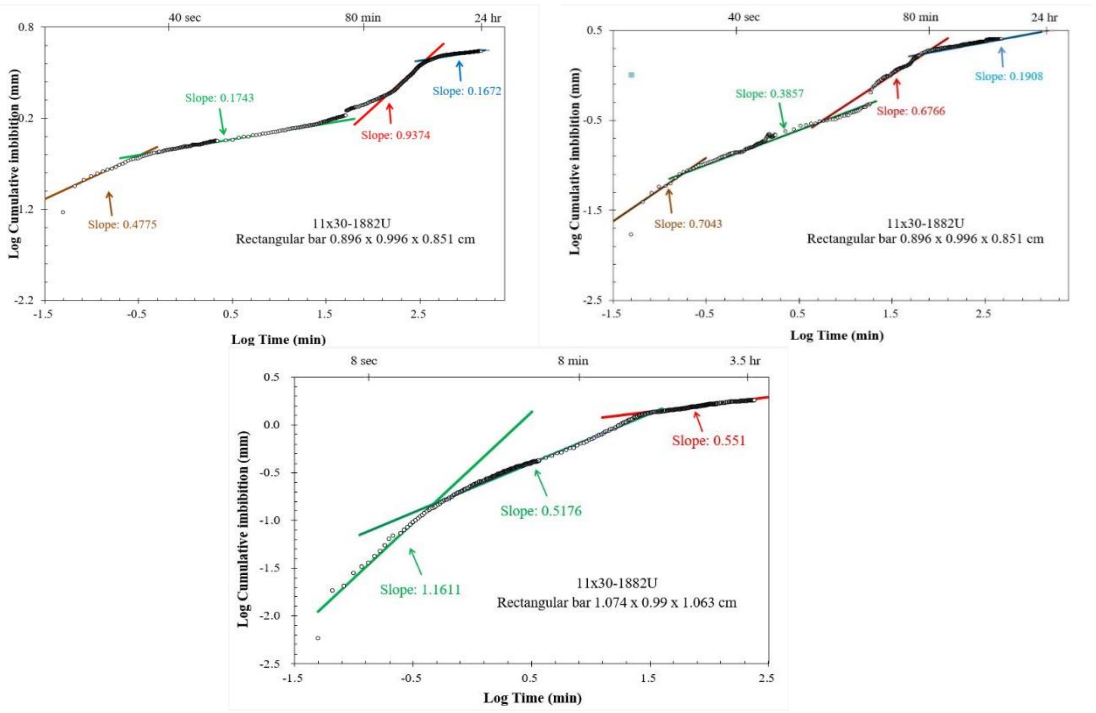

Figure 33. Fluid imbibition curve from left (DIW at 24 hrs testing duration), right (DIW 8 hrs), bottom (2DT 4 hrs) for Sample 11x30-1882U

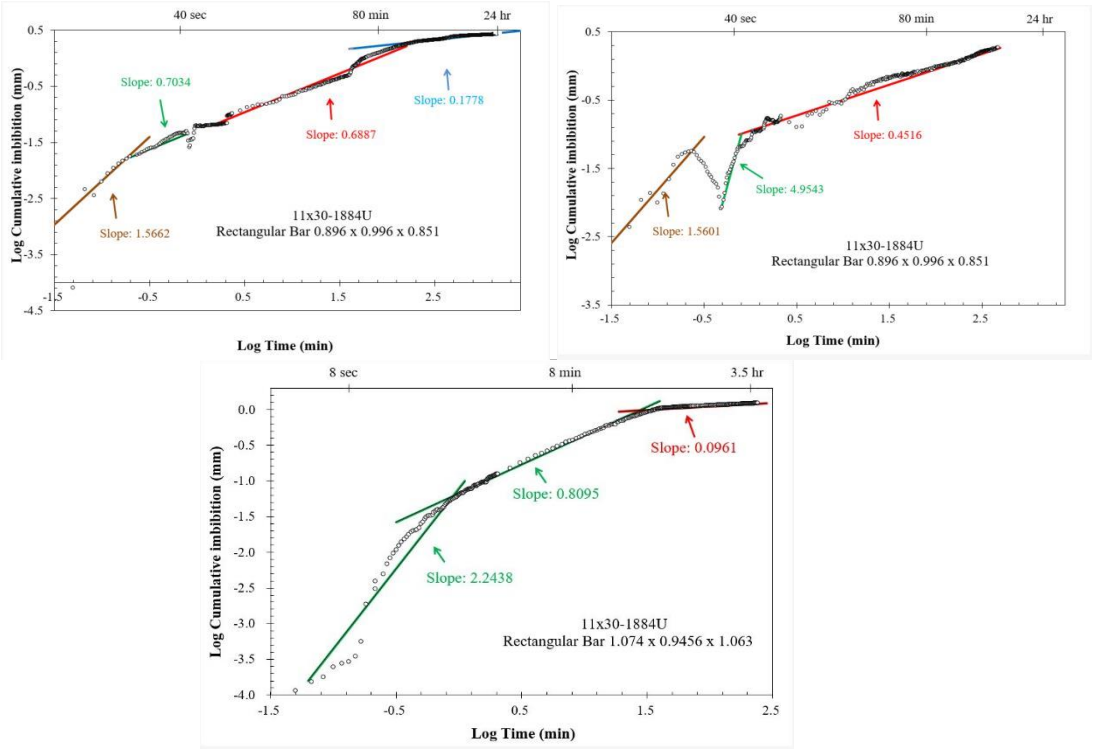

Figure 34. Fluid imbibition curve from left (DIW 24 hrs), right (DIW 8 hrs), bottom (2DT 4 hrs) for Sample 11x30-1884U

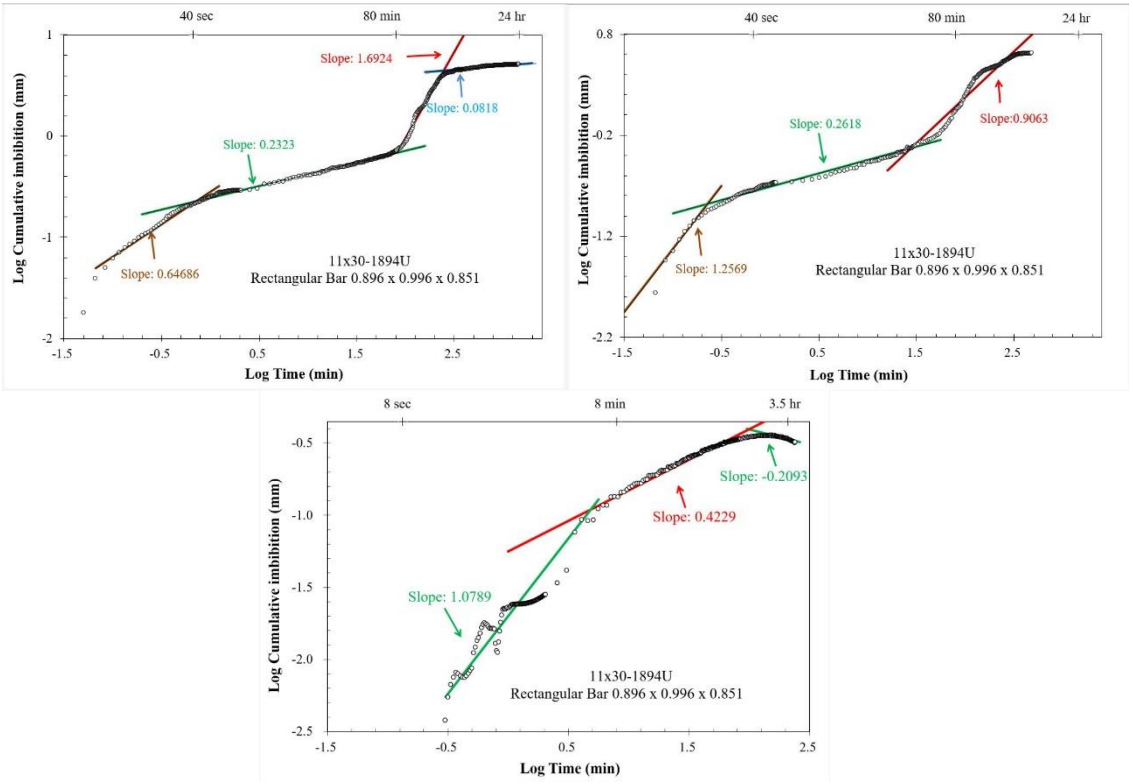

Figure 35. Fluid imbibition curve from left (DIW 24 hrs), right (DIW 8 hrs), bottom (2DT 4 hrs) for 11x30-1894U

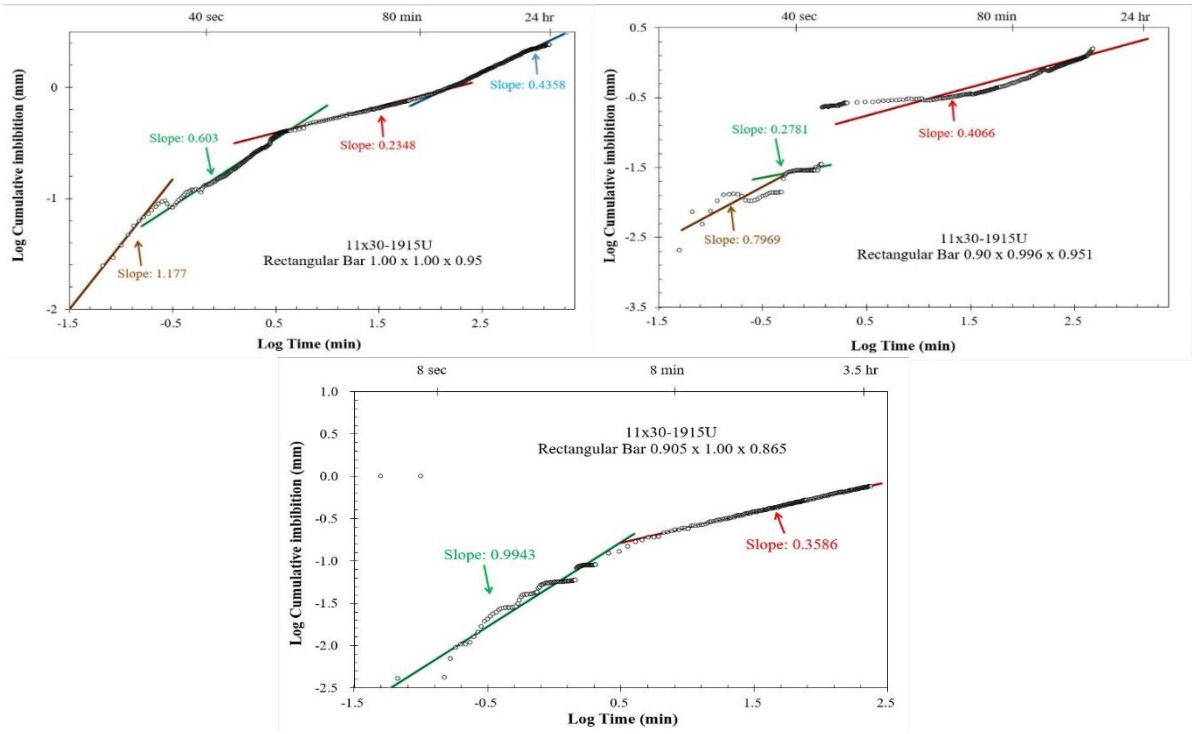

Figure 36. Fluid imbibition curve from left (DIW 24 hrs), right (DIW 8 hrs), bottom (2DT 4 hrs) for 11x30-1915U

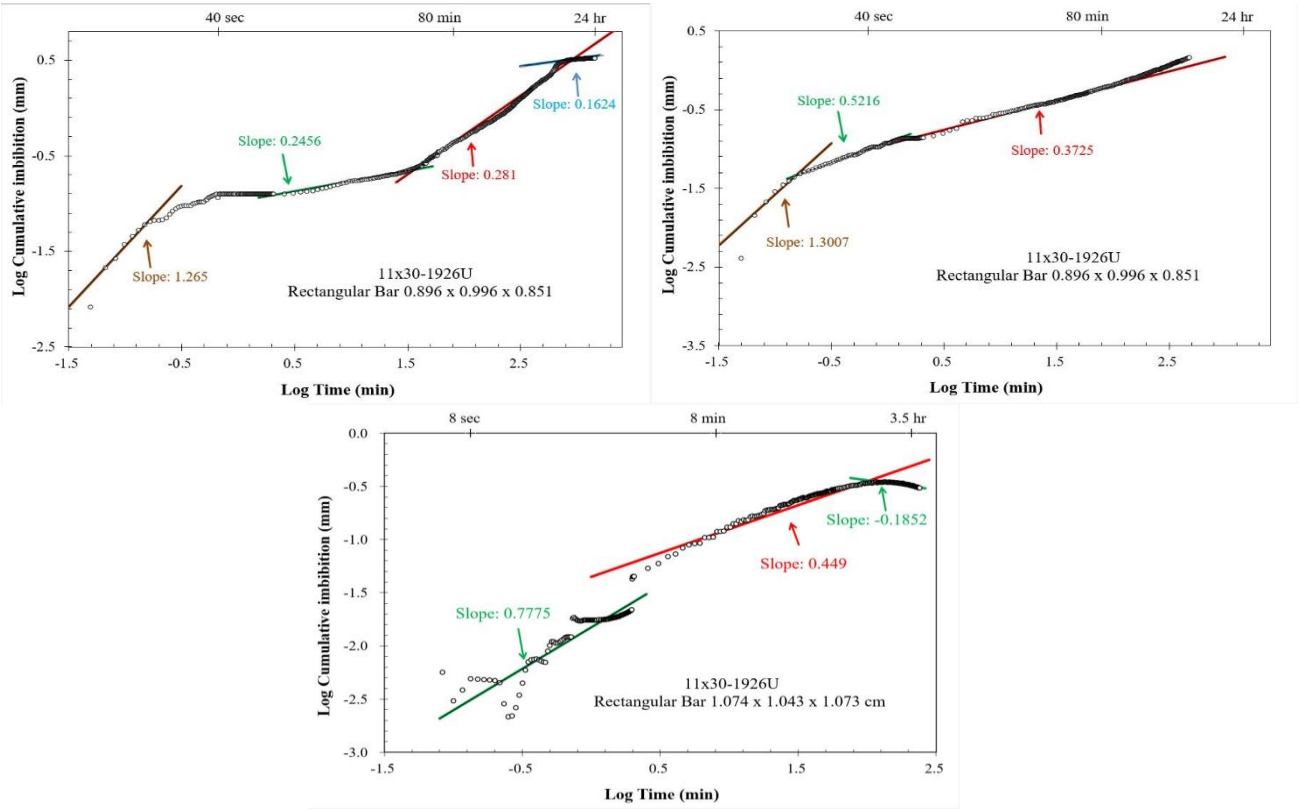

Figure 37. Fluid imbibition curve from left (DIW 24 hrs), right (DIW 8 hrs), bottom (2DT 4 hrs) for Sample 11x30-1926U

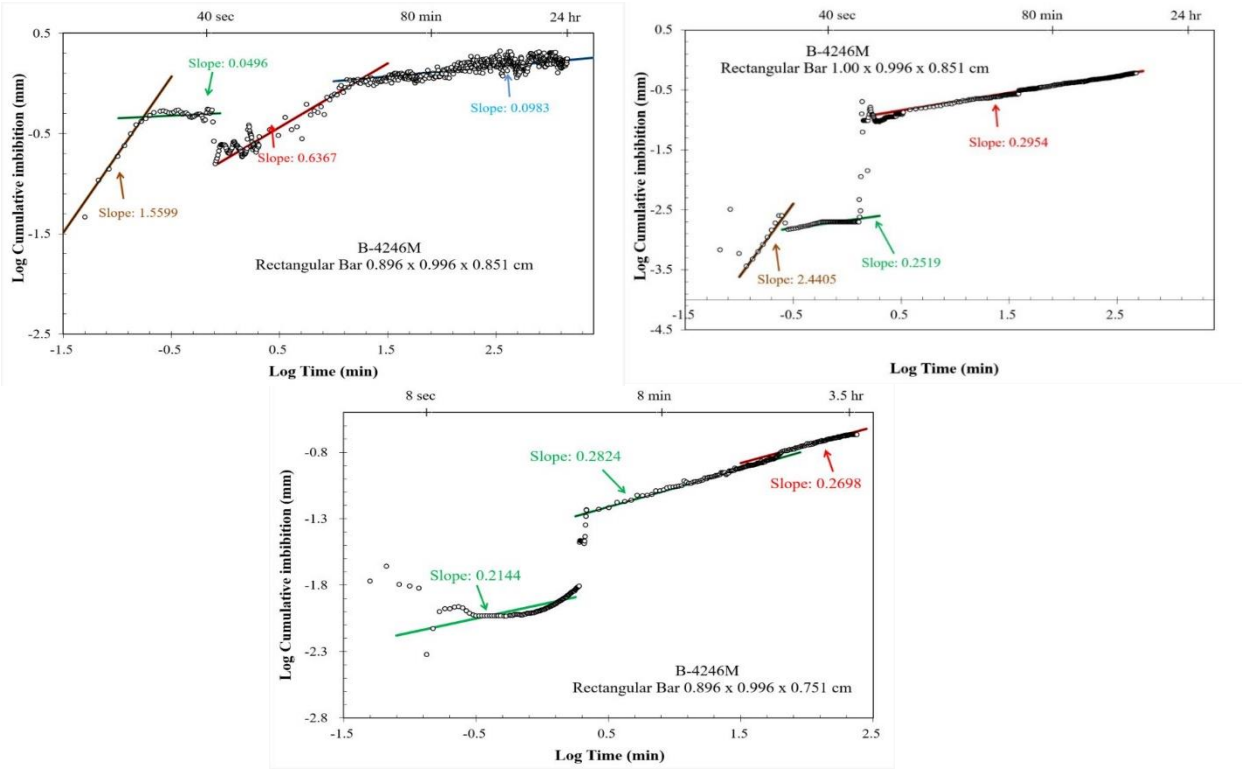

Figure 38. Fluid imbibition curve from left (DIW 24 hrs), right (DIW 8 hrs), bottom (2DT 4 hrs) for Sample B-4246M

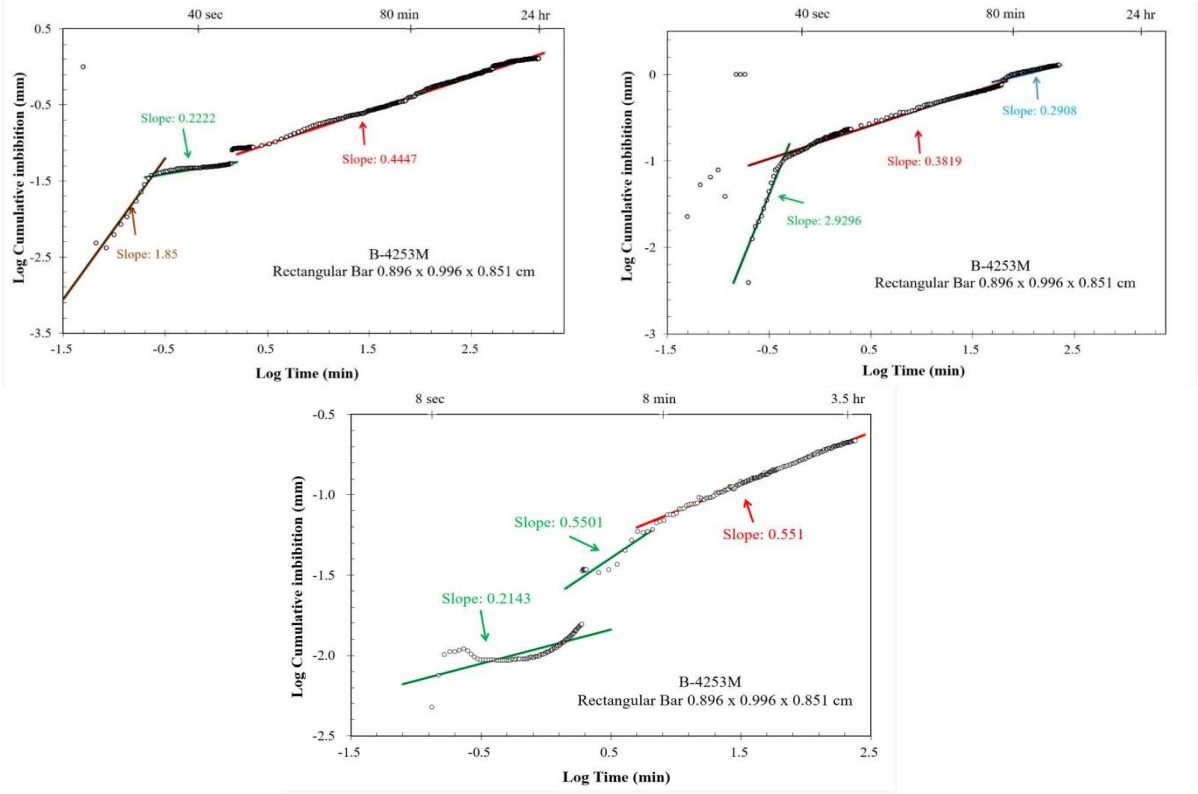

Figure 39. Fluid imbibition curve from left (DIW 24 hrs), right (DIW 8 hrs), bottom (2DT 4 hrs) for Sample B-4253M

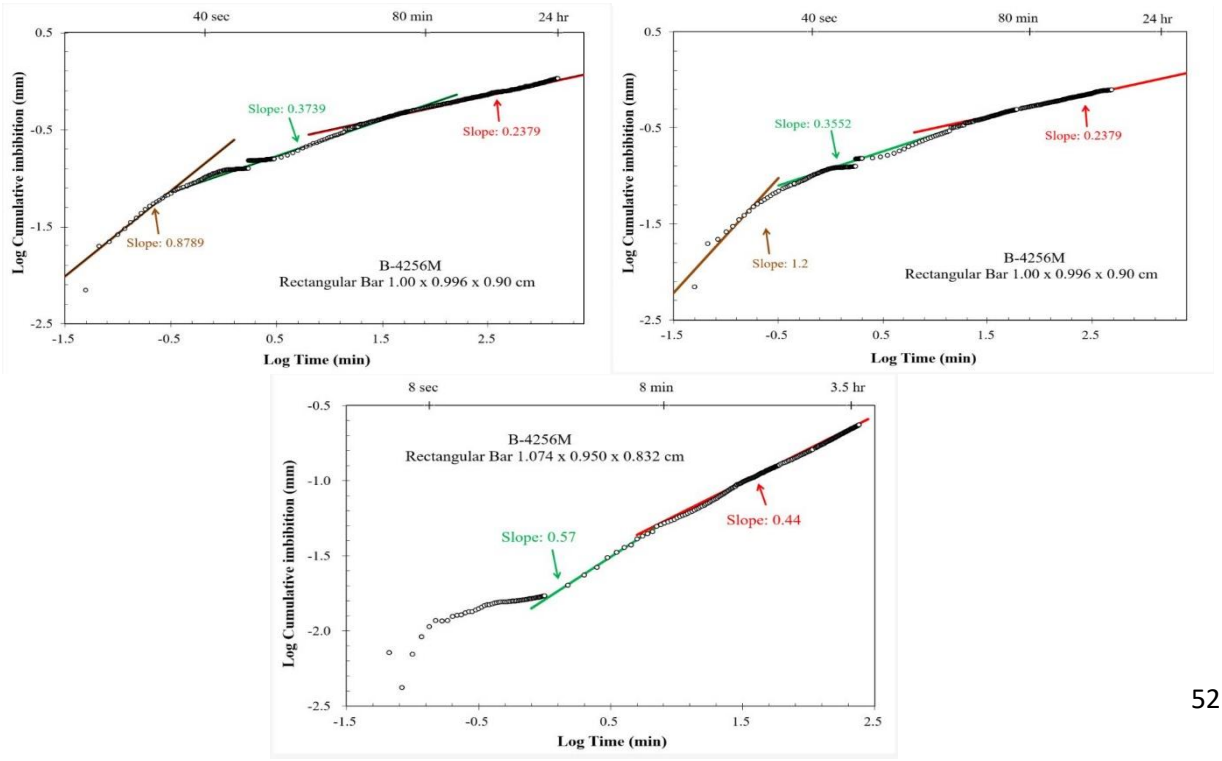

Figure 40. Fluid imbibition curve from left (DIW 24 hrs), right (DIW 8 hrs), bottom (2DT 4 hrs) for Sample B-4256M

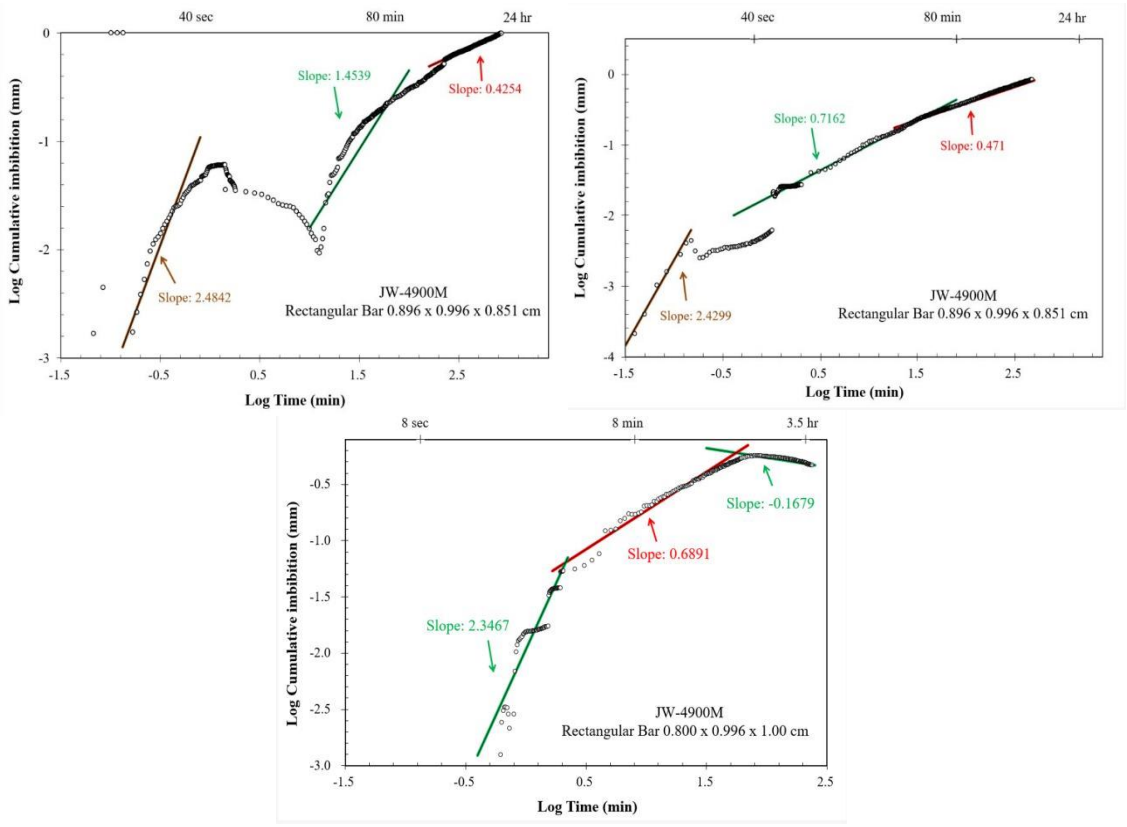

Figure 41. Fluid imbibition curve from left (DIW 24 hrs), right (DIW 8 hrs), bottom (2DT 4 hrs) for Sample JW2-4900M

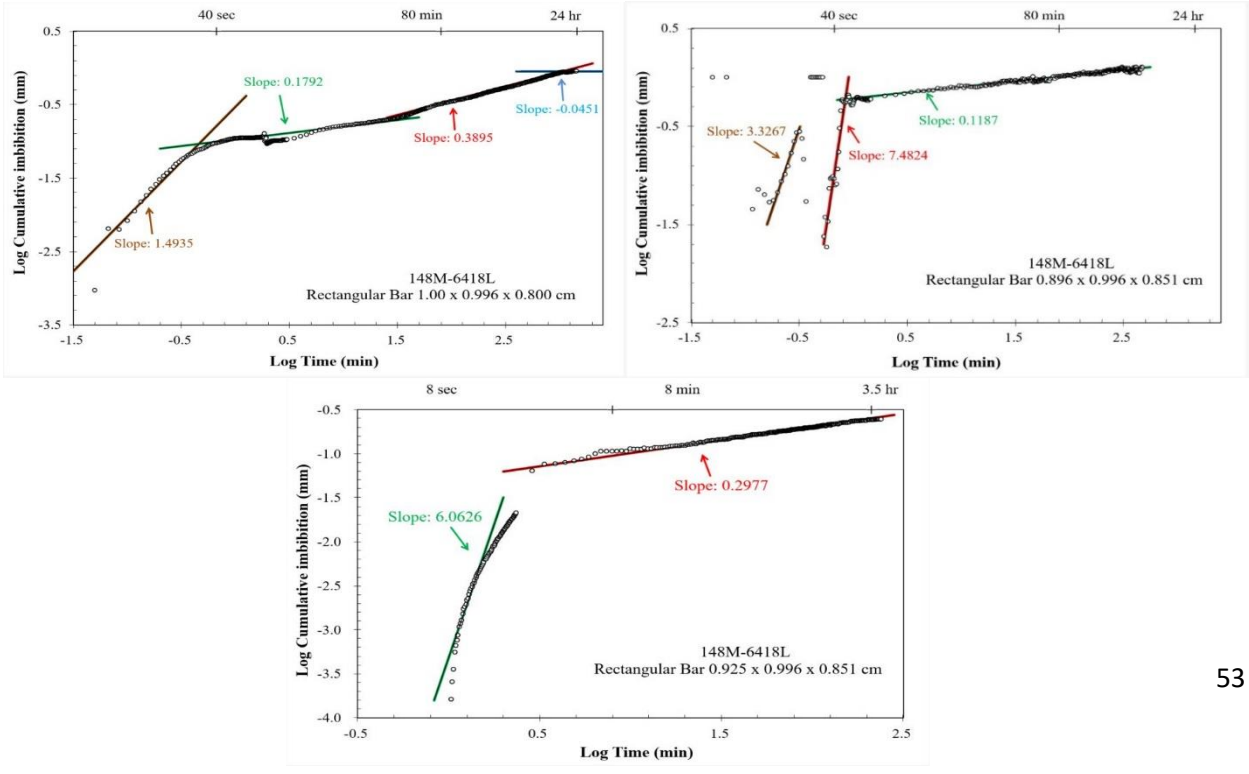

Figure 42. Fluid imbibition curve from left (DIW 24 hrs), right (DIW 8 hrs), bottom (2DT 4 hrs) for Sample 148M-6418L

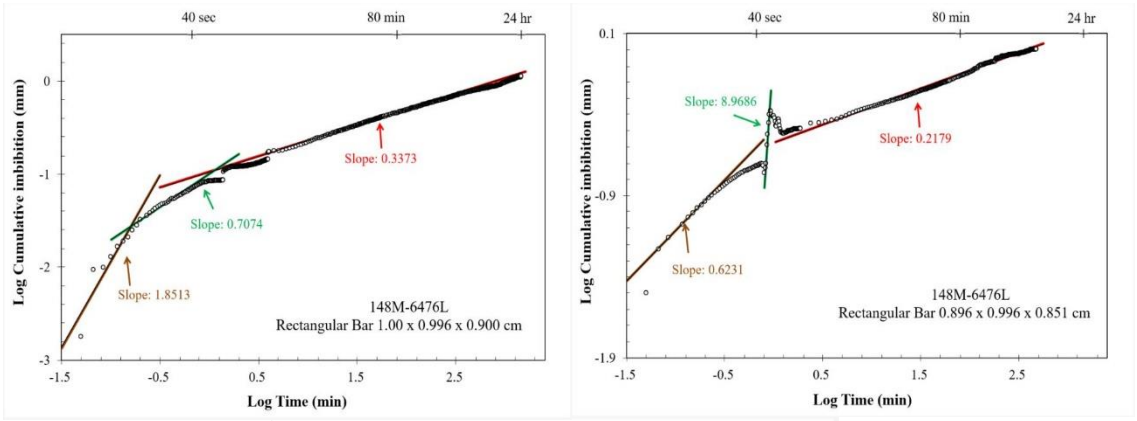

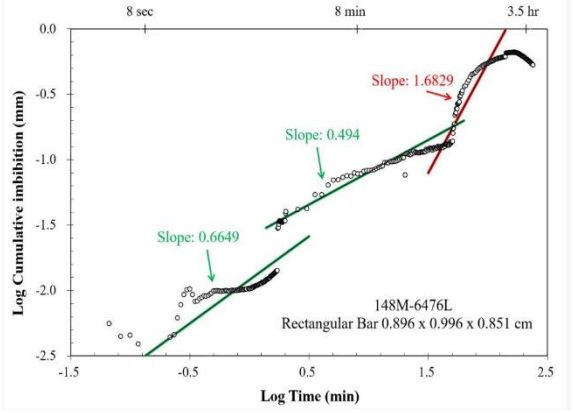

Figure 43. Fluid imbibition curve from left (DIW 24 hrs), right (DIW 8 hrs), bottom (2DT 4 hrs) for Sample 148M-6476L

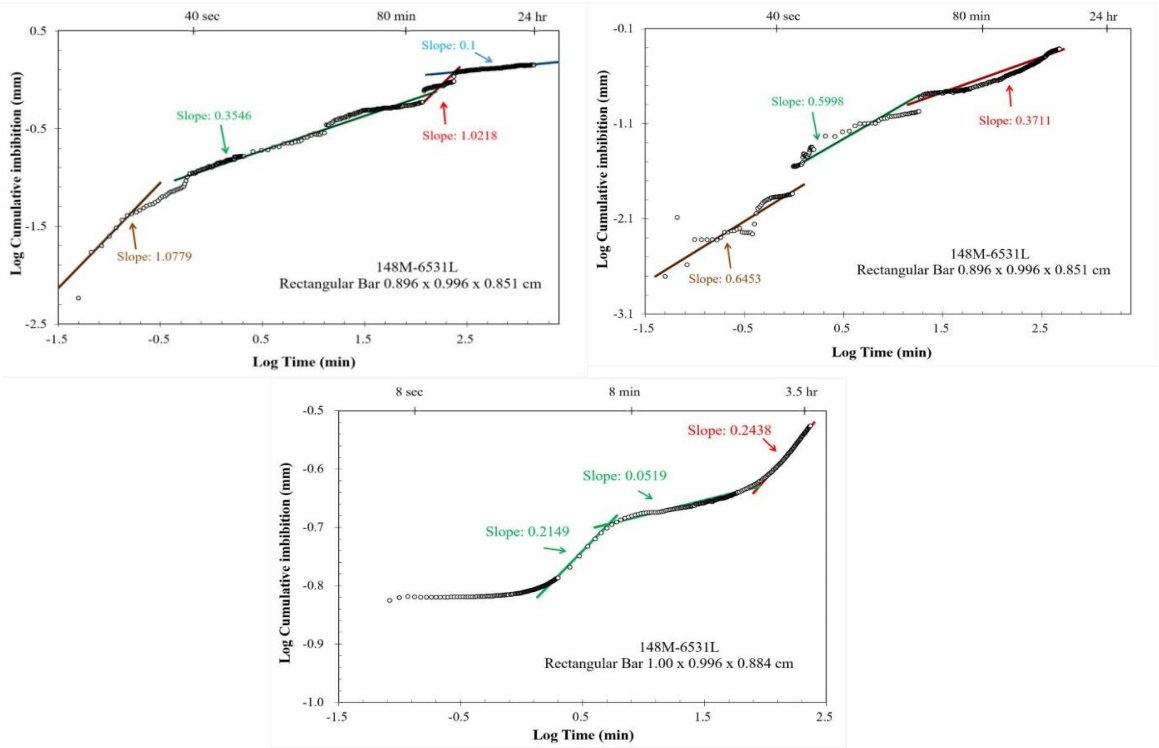

Figure 44. Fluid imbibition curve from left (DIW 24 hrs), right (DIW 8 hrs), bottom (2DT 4 hrs) for Sample 148M-6531L

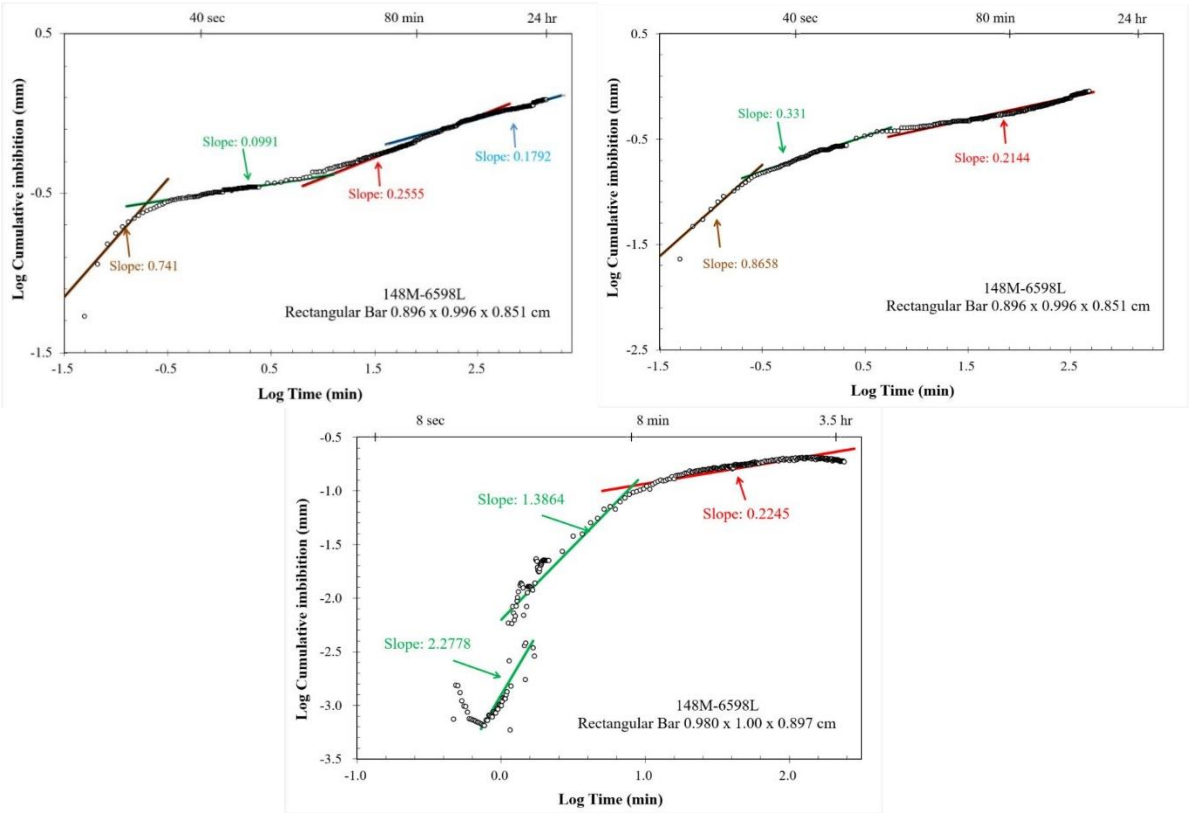

Figure 45. Fluid imbibition curve from left (DIW 24 hrs), right (DIW 8 hrs), bottom (2DT 4 hrs) for Sample 148M-6598

Sample ID	Fluid Type	Wall & Edge Slope	Interior Stage Slope	Connectivity
11x30-1882U	DI Water	0.1743	0.9374	High
11x30-1884U	DI Water	0.7034	0.6887	High
11x30-1894U	DI Water	0.2323	1.6926	High
11x30-1915U	DI Water	0.603	0.2348	Low
11x30-1926U	DI Water	0.2456	0.281	Intermediate
B-4246M	DI Water	0.0496	0.6367	High
B-4253M	DI Water	0.2222	0.4447	Intermediate
B-4256M	DI Water	0.3739	0.2379	Low
JW-4900M	DI Water	1.4539	0.4254	Intermediate
148M-6418L	DI Water	0.1792	0.3895	Intermediate
148M-6476L	DI Water	0.7074	0.3373	Intermediate
148M-6531L	DI Water	0.3546	1.0218	High
148M-6598L	DI Water	0.0991	0.2555	Low

Sample ID	Fluid Type	Wall & Edge Slope	Interior Stage Slope	Connectivity
11x30-1882U	DI Water	0.3857	0.6766	High
11x30-1884U	DI Water	4.9543	0.4516	Intermediate
11x30-1894U	DI Water	0.2618	0.9063	High
11x30-1915U	DI Water	0.2781	0.4066	Intermediate
11x30-1926U	DI Water	0.5216	0.3725	Intermediate
B-4246M	DI Water	0.2516	0.2954	Intermediate
B-4253M	DI Water	0.3819	0.2908	Intermediate
B-4256M	DI Water	0.3552	0.2379	Low
JW-4900M	DI Water	0.7162	0.471	Intermediate
148M-6418L	DI Water	7.4824	0.1187	Low
148M-6476L	DI Water	8.9686	0.2179	Low
148M-6531L	DI Water	0.5998	0.3711	Intermediate
148M-6598L	DI Water	0.331	0.2144	Low

Table 8. Compilation of fluid imbibition data from top (DIW 24 hrs) and bottom (DIW 8 hrs)

Sample ID	Fluid Type	Wall & Edge Slope	Interior Stage Slope	Connectivity
11x30-1882U	2DT	0.5176	0.5176	High
11x30-1884U	2DT	2.2438	0.8095	High
11x30-1894U	2DT	1.0789	0.4229	Intermediate
11x30-1915U	2DT	0.9943	0.3586	Intermediate
11x30-1926U	2DT	0.7775	0.449	Intermediate
B-4246M	2DT	0.2144	0.2824	Intermediate
B-4253M	2DT	0.2143	0.5501	High
B-4256M	2DT	0.57	0.44	Intermediate
JW-4900M	2DT	2.3467	0.6891	High
148M-6418L	2DT	6.0626	0.2977	Intermediate
148M-6476L	2DT	0.6649	0.494	Intermediate
148M-6531L	2DT	0.2149	0.0519	Low
148M-6598L	2DT	2.2779	1.3864	High

Table 9. Compilation of fluid imbibition data for 2DT at an experimental duration of 4 hrs

Discussion

Mineralogy of the Upper Mancos Shale

Previous studies state that the carbonate content increases in the northeastern part of the San Juan Basin, while the more silica rich facies are found in the southwest region of the Basin. By comparing the carbonate content of Burnham 1 with JW2 and 11x30 with 148M, only the latter can be confirmed that the carbonate content does increase northeastward of the Basin (Figure 45). Samples in Well Burnham 1 surprisingly have a high percentage of carbonate, even more than Well 148M, which is situated at the northeast region of the Basin. On the other hand, the results show that the majority of the samples of Well 11x30, which is situated in the southwest region of the Basin, have the highest value of silica mineral (quartz) (Figure 46), which therefore confirms the previous studies. All the 13 samples seem to have high clays content, ranging from 32.4% to 60.4%.

According to Zhang et al. (2017), clay-abundant shale formations have a positive influence on gas storage potential, because the laminated structures of fine clay particles can

create high total surface area and high porosities, which is great for gas adsorption. However, clay-abundant formations have significant amounts of water due to the high affinity of clay contents to water molecules, and high water contents contribute to the reduction of gas storage capacity by occupying potential sorption sites in the shale mass and blocking the small pore throats. The average of quartz and feldspar, clays, and carbonate contents from each well were taken to construct a lithofacies classification.

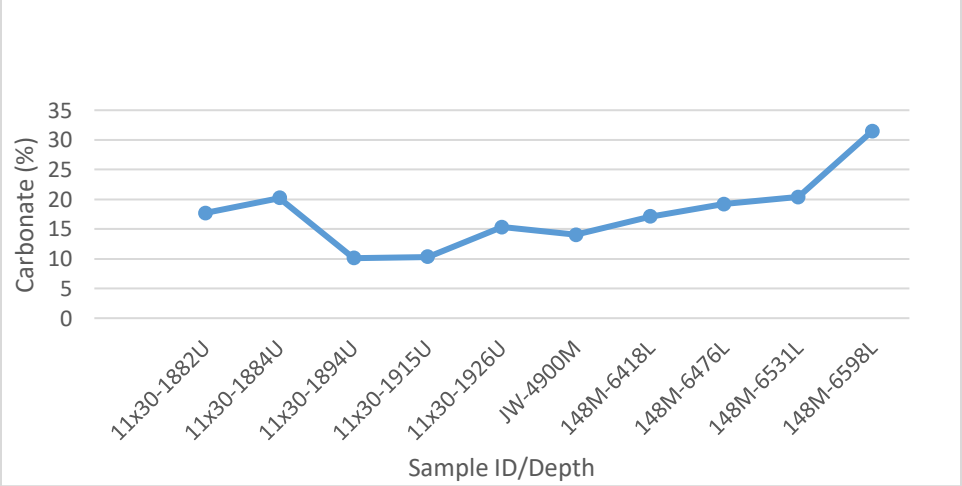

Figure 46. Carbonate increases from southwest to northeast of the San Juan Basin

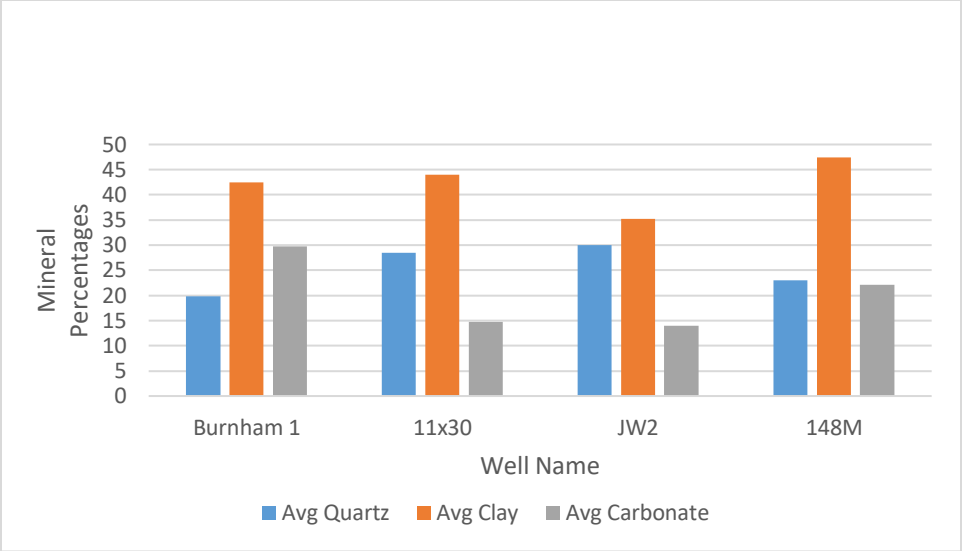

Figure 47. Average of quartz, carbonate, clays components among four wells

TOC and pyrolysis analyses of the Upper Mancos Shale

Kerogen types are determined from the Pseudo Van Krevelen plot of oxygen index vs. hydrogen index (Figure 21) and kerogen quality plot of TOC vs. S2 (Figure 20). The Pseudo Van Krevelen plot shows all samples have a kerogen types ranging from Type I to Type III, with the majority of the samples falling in to Type II and III kerogen, whereas the TOC vs. S2 plot shows the kerogen quality ranging from Type II/III Oil to Gas Prone to Dry Gas Prone, with all except for three samples are Type III Gas Prone.

Calculated vitrinite reflectance (% Ro), a way to determine the thermal maturation, was done by using the equation in Jarvie et al. (2001; 2012) reported for the Barnett Shale: Ro = 0.0180 x (T_{max} - 7.16). The % Ro ranges from 0.56 to 1.10 which is quite consistent with results from previous studies of approximately 0.65–1.5 (Figure 47). The maturation increases to the northeast with increasing depths (Broadhead, 2013). In previous studies, the average TOC for the Mancos Shale was found to range of 1% - 2%, and increases to the northeast, which is also

consistent to the result in this research with an average of 1.38% TOC (Figure 48)

. However, according to Broadhead (2013), there are naturally fractured and oil filled Mancos Shales along the eastern and western flank of the Basin, which is confirmed by the high TOC value for Well Burnham 1 located at the western side of the Basin.

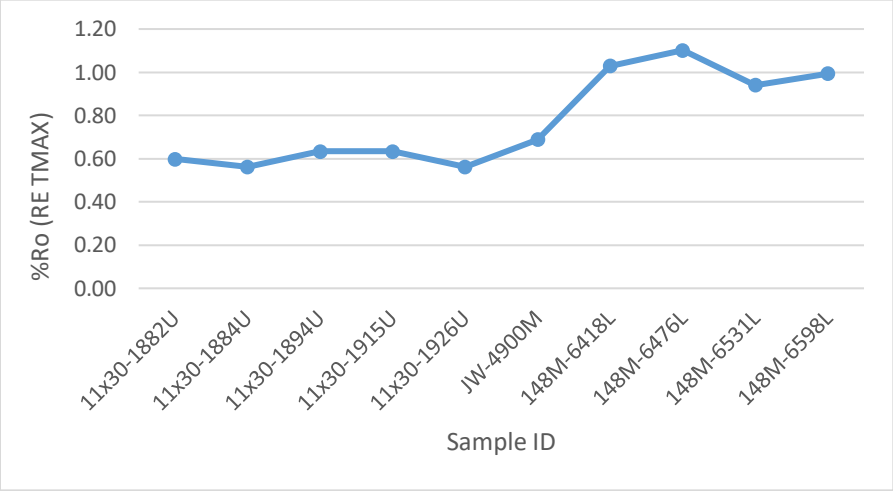

Figure 48. %Ro increases from southwest to northeast of the Basin with increasing depths

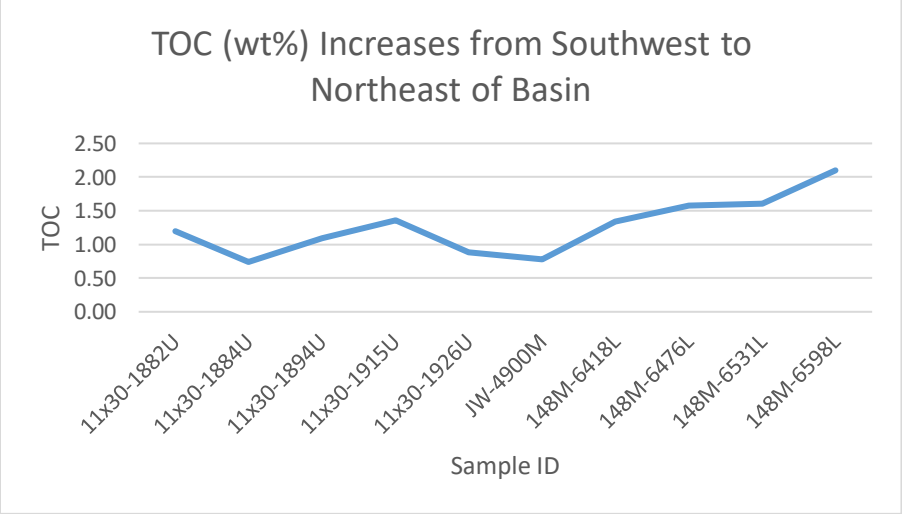

Figure 49. TOC increases from southwest to northeast of basin, excluding B-4253M and B-4256M.

Pore structure characteristics from N_2 physisorption

The commercial production of shale hydrocarbons has been increasing for the past decade and naturally there have been more demands in understanding the pore structure of shales. In this thesis work, the nitrogen gas at liquid nitrogen temperature is adsorbed into the samples and the resulting isotherm shows the mechanism of pore filling, which can be used to deduce the pore volume and area distributions.

According to the isotherm result, the samples contain both macropores (>50 nm) and mesopores (2-50 nm). From the DFT pore size distribution plot (Figure 49), samples from Well 11x30 exhibits all types of pores, with the highest percentage of pore volume ranging from 10 nm to 50 nm, followed by 50 nm – 100nm range; Well Burnham 1 again exhibits all types of pores, dominated by 10 nm-50 nm, 50 nm to 100 nm, and 100 nm – 126 nm; Well JW2 exhibits all types of pores and is controlled by 10 nm- 50 nm; and Well 148M exhibits all types of pores, with pore volumes controlled by 10 nm-50 nm. The overall results show that samples from all wells are microporous, mesoporous, and macroporous, with dominant pore volumes of 10 nm - 50 nm.

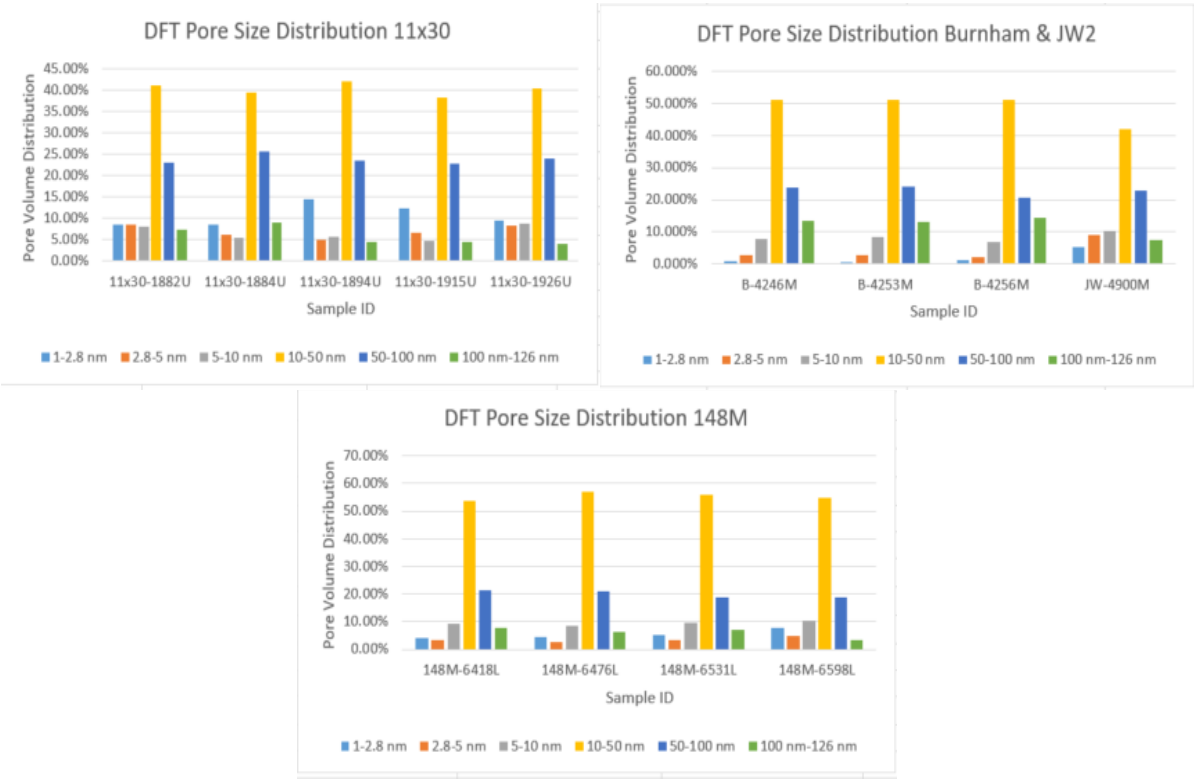

Figure 50. DFT pore size distribution for each samples

Fluid-rock interaction and pore connectivity

The behavior of a fluid-rock interaction varies by the type of fluid used and also the composition of the rock itself. By using the contact angle method, it is possible to have a quantitative assessment on the wetting characteristic of the Mancos Shale. In addition, the imbibition test has the ability of assessing the pore connectivity of the samples by altering the fluids used, in this case, DIW (hydrophilic fluid) and 2DT (hydrophobic fluid).

From the wettability test through contact angle method, the Mancos Shale samples are moderately strongly water wet and the results with 2DT show that the samples are oil wet. Overall, all the samples have a mixed wettability, where it is moderately strongly water wet and strongly oil wet. In the case of mixed wettability, oil has displaced water from some of the surfaces but remains in the centers of water wet pores. Through the fluid imbibition test, the 24

hour DIW test yield an overall result of high connectivity characteristics, with an average connectivity slope of 0.583, 8 hours DIW yield an intermediate connectivity, with an average connectivity slope of 0.387, and the 4 hours 2DT test yield high connectivity, with an average connectivity slope of 0.519. Therefore, these experiments show that the samples have intermediate to well connectivity with hydrophilic fluid and well connectivity pore network with hydrophobic fluid, which are consistent with the contact angle result.

Density and Porosity

The variations in the particle density are due to the presence of heavier minerals (such as iron oxides) or organic matter (which has a low density and reduces the overall particle density value). The relationship of bulk density and porosity is reciprocal. As one increases, the other decreases. As mentioned earlier, clay minerals have a strong affinity for water. The use of conventional water-based fracking fluid therefore causes the initiation of clay minerals (e.g., smectite, illite) and water molecules interactions, creating a significant swelling in the formation. This swelling may cause a significant reduction in shale mass pore space. Particularly after the hydro-fracking process, a considerable amount of residual water is trapped inside the created hydraulic fractures and natural fractures and the interaction of this water with formation clay minerals greatly reduces the formation porosity and eventually its permeability. Figure 50 shows that, in general, the porosities from the helium pycnometry and 2DT vacuum saturation decreases with depth. Figures 51-52 show that there is an inverse relationship between porosity and bulk density from the helium pycnometry test.

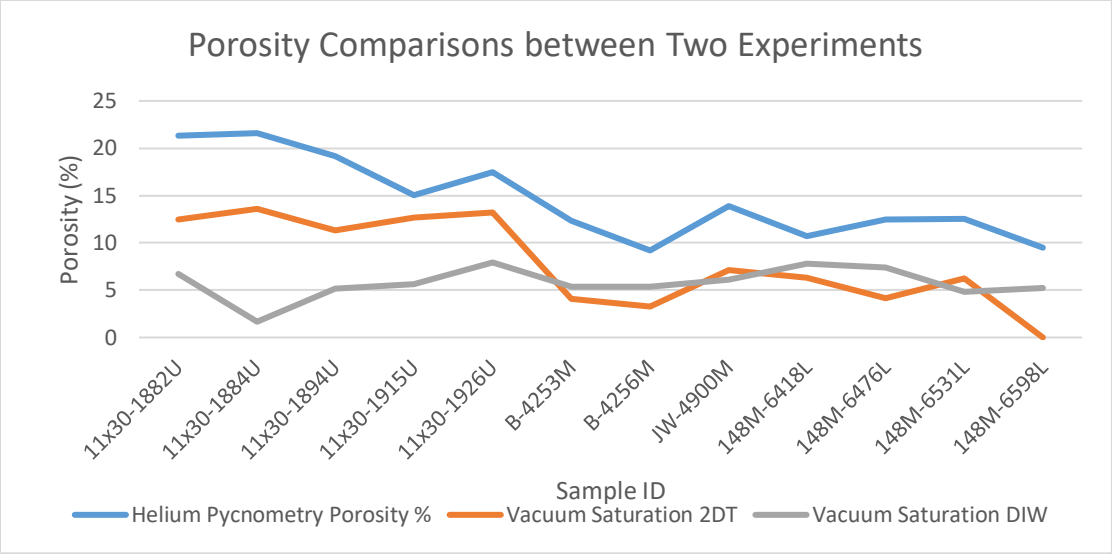

Figure 51. Porosity comparisons between helium pycnometry and vacuum saturation; 2DT vacuum saturation and helium pycnometry demonstrate similar trend.

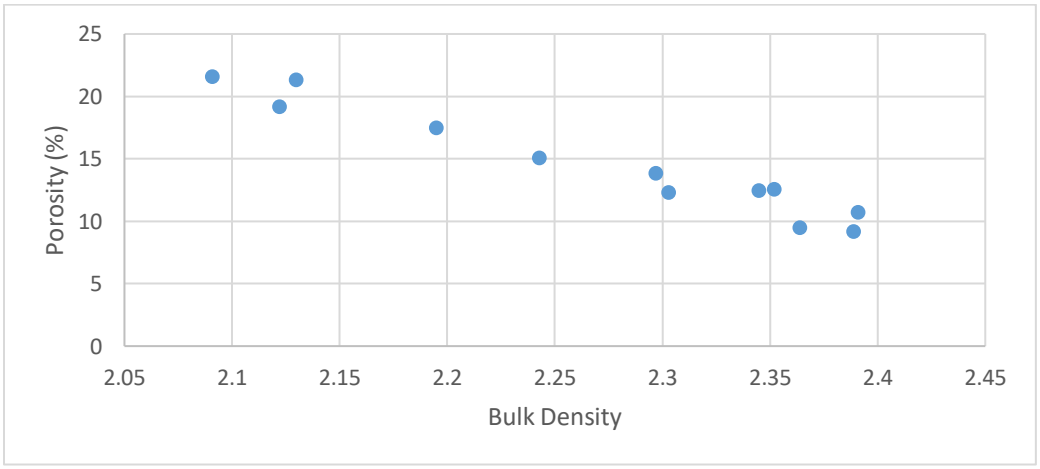

Figure 52. An inverse relationship between porosity and bulk density from the helium pycnometry test.

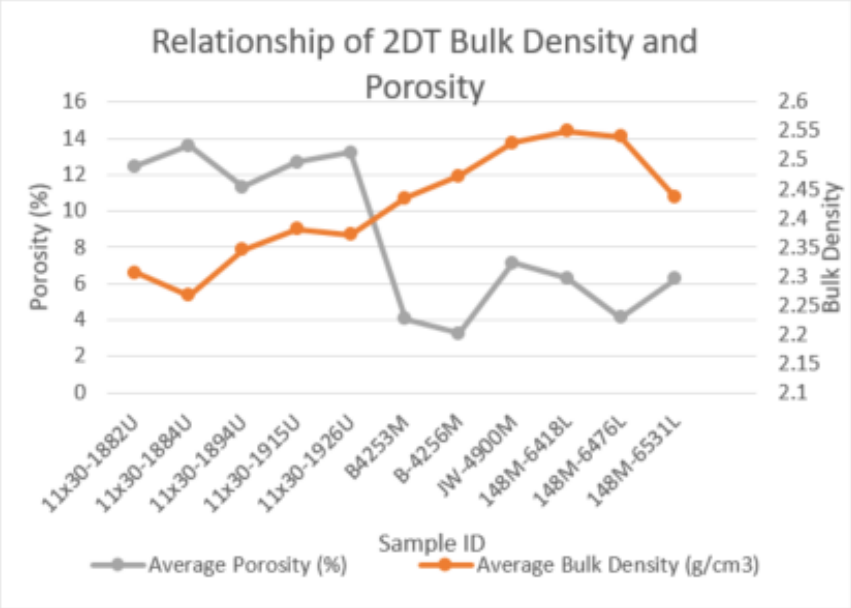

Figure 53. An inverse relationship between porosity and bulk density from the 2DT vacuum saturation test

Conclusion and Recommendation

XRD analyses were performed to identify the mineralogy of 13 samples of Mancos Shale and it detects five different types of minerals, which are quartz, feldspar, carbonates, sulfides, and clays. Carbonate content increases in the northeastern part of the San Juan Basin, while the more silica-rich facies are found in the southwest region of the Basin. N_2 physisorption show that all the samples are mesoporous and macroporous, except for the samples in well 11x30, which is also microporous (<2 nm), with most of the pore volumes are controlled by 25.25 nm – 93.13 nm pore throat sizes. The majority of the samples was evenly distributed between Argillaceous Siliceous Mudstone (11x30-1884U, 11x30-1894U, 11x30-1926U, JW-4900M, 148M-6418L, 148M-6476L) and Mixed Mudstone (11x30-1884U, B-4246M, B-4253, B-4256M, 148M-6531L, 148M-6598L) with six samples each. Only one sample (11x30-1915U) falls in the Mixed Argillaceous Mudstone classification.

The maturation by Calculated Vitrinite Reflectance (% Ro) from T_{max} and TOC increases from the southwest to northeast region of the Basin, and there are high TOC contents on the east and west flank of the Basin. The fluid imbibition experiment shows that the samples have intermediate to well connectivity with hydrophilic fluid and well connectivity pore network with hydrophobic fluid, whereas the contact angle results show that all the samples are moderately strongly water wet and strongly oil wet. From various methods of determining density and porosity, the helium pycnometry and 2DT vacuum saturation results show that the porosity decreases with depth, and there is an inverse relationship between porosity and bulk density from the 2DT vacuum saturation and helium pycnometry test. One possible reason for the DIW vacuum saturation test did not yield similar result is the high quantity of clays in the samples, where water would cause swelling and fracturing of the sample, thus affecting the pore structure.

In order to better understand the mineralogical and organic geochemical characteristics that control pore-size distribution, additional tests like mercury intrusion porosimetry, nano-CT, focused ion beam-scanning electron microscopy and gas diffusion would be suitable to paint a more complete picture of pore structure.

Acknowledgments

I would like to thank my advisor, Dr. Qinhong Hu for his guidance and encouragement throughout my studies at UTA, without whom, I would not have made it to this stage. I would also like to thank my Dr. Majie Fan and Dr. Nathan Brown for taking the time to be part of my committee members.

Many thanks to my peers from Dr. Hu's research group, Qiming Wang, Chen Zhao, and Prince Oware, to name a few, who had assisted me in my lab research.

Last, but not least, I would like to thank my parents for their undying love and constant support.

References

Al-Arfaj, M., & Al-Kharaa, H. (2017). Understanding Shale Petrophysics Helps in Drilling Stable Boreholes: Case Studies. *SPE/IATMI Asia Pacific Oil & Gas Conference and Exhibition* (pp. 1-34). Jakarta: Society of Petroleum Engineers.

Assessment of Undiscovered Oil and Gas Resources in the MancosMenefee Composite and Underlying Todilto Total Petroleum Systems of the. (2020, November). Retrieved from usgs.gov: https://pubs.usgs.gov/fs/2020/3049/fs20203049.pdf

Barrett, E. P., L. G. Joyner, and P. P. Halenda, 1951, The determination of pore volume and area distributions in porous substances — 1. Computations from nitrogen isotherms: Journal of the American Chemical Society, 73, 373–380.

Borysenko, A., Clennell, B., Sedev, R., Burgar, I., Ralston, J., Raven, M., . . . Liu, K. (2009). Experimental investigations of the wettability of clays and shales. *Journal of Geophysical Research- Solid Earth*, 1-11.

Brian, B. S., Price, L., & Editors. (2002). New Mexico's Energy, Present and Future: Policy, Production, Economics, and the Environment. *Decision Makers Field Conference* (pp. 27-31). Soccoro: New Mexico Bureau of Geology and Mining Resources .

Broadhead, R. F. (2015). The Upper Mancos Shale in the San Juan Basin: Three plays, Conventional and Unconventional. *Search and Discovery*, 1-39.

Craigg, S. D. (2001). Geologic Framework of the San Juan Structural Basin of New Mexico, Colorado, Arizona, and Utah, With Emphasis on Triassic Through Tertiary Rocks. *U.S. Geological Survey Professional Paper 1420*, 1-81.

Dandekar, A. Y. (2013). *Petroleum Reservoir Rock and Fluid Properties.* Boca Raton: Taylor & Francis.

Engler, T. W., Brister, B. S., Chen, H.-Y., & Teufel, L. W. (2001). *Oil and Gas Resource Development for San Juan Basin, New Mexico: A 20- Year, Reasonable Foreseeable Development (RFD) Scenario Supporting the Resource Management Plan for the Farmington Field Office, Bureau of Land Management.* Albuquerque: U.S. Department of the Interior Bureau of Land Management.

Hu, M., Persoff, P., & Wang, J. (2001). Laboratory Measurement of Water Imbibition into Low-Permeability Welded Tuff. *Journal of Hydrology*, 64-78.

Hu, Q. P., & Wang, J. (2001). Laboratory Measurement of Water Imbibition into Low Permeability Welded Tuff. *Journal of Hydrology*, 64-78.

Hu, Q., Ewing, R. P., & Dultz, S. (2012). Low Pore Connectivity in Natural Rock. *Hournal of Contaminant Hydrology*, 76-83.

Hu, Q., Kalteyer, R., Wang, J., & El-Sobky, H. F. (2019). Nanopetrophysical characterization of the Mancos Shale Formation in the San Juan Basin of northwestern New Mexico, USA. *Interpretation*, SJ45-SJ65.

Huffman Jr., A. C. (1987). *Petroleum Geology and Hydrocarbon Plays of the San Juan Basin Petroleum Province.* Denver: U.S. Geological Survey.

Kalteyer, R. (2017). *Nano Petrophysics Characterization of the Mancos Shale Formation in the San Juan Basin of Northwestern New Mexico, USA.* Arlington: University of Texas at Arlington.

Leung, M. (2018). *Detailed Thin-Bedded Facies Analysis of the Upper Mancos Shale.* Hamilton: McMaster University.

Liu, H., Zhang, L., & Seaton, N. A. (1993). Sorption Hysteresis as a Probe of Pore Structure. *Langmuir*, 2576-2582.

Molenaar, C. (1977). Stratigraphy and Depositional History of Upper Cretaceous Rocks of the San Juan Basin Area, New Mexico And Colorado, With a Note on Economic Resources. *28th Field Conference* (pp. 159-165). Socorro: New Mexico Geol. Soc. .

Morsy, S. (2014). *Experimental and Simulation Study of Improved Oil Recovery in Shale Formations* . Lubbock: Texas Tech University.

Neimarka, A. V., Y. Z. Lin, P. I. Ravikovitch, and M. Thommes, 2009, Quenched solid density functional theory and pore size analysis of micro-mesoporous carbons: Carbon, 47, 1617–1628,

New Mexico Field Production of Crude Oil. (2021, October 29). Retrieved from U.S. Energy Information Administration: https://www.eia.gov/dnav/pet/hist/LeafHandler.ashx?n=PET&s=MCRFPNM2&f=A

New Mexico Natural Gas Flaring and Venting Regulations. (2019, May). Retrieved from fossil.energy.gov: https://www.energy.gov/sites/prod/files/2019/08/f66/New%20Mexico.pdf

New Mexico Natural Gas Gross Withdrawal. (2021, October 29). Retrieved from U.S. Energy of Information Administration: https://www.eia.gov/dnav/ng/hist/n9010nm2a.htm

Seaton, N. (1991). Determination of the Connectivity of Porous Solids from Nitrogen Sorption Measurements. *Chemical Engineering Science*, 1895-1909.

Sondergeld, C. H., Newsham, K. E., Comisky, J. T., Rice, M. C., & Rai, C. S. (2010). Petrophysical Considerations in Evaluating and Producing Shale Gas Resources. *SPE Unconventional Gas* (pp. 1-34). Pittsburgh: Society of Petroleum Engineers.

Wood, D. A., and B. Hazra, 2017, Characterization of organic- rich shales for petroleum exploration and exploitation: A review — Part 1: Bulk properties, multi-scale geometry and gas adsorption: Journal of Earth Science,

Wright, A. F. (1979). Bibliography of Geology and Hydrogeology, San Juan Basin, New Mexico, Colorado, Arizona, and Utah. *Geological Survey Bulletin 1481*, 1-132.

Zhang, C., Pathegama Gamage, R., Perera, M., & Zhao, J. (2017). Characteristics of Clay-Abundant Shale Formations: Use of CO2 for Production Enhancement. *Energies 10*, 1-37.

Zhao, C., W. Zhou, Q.H. Hu, H. Xu, T. Zhang, and C. Zhang. 2021. Porosity measurement of granular rock samples by modified bulk density analyses with particle envelopment. *Marine and Petroleum Geology*, 133, 105273. DOI: 10.1016/j.marpetgeo.2021.105273.